Department of Physics and Astronomy

Heidelberg University

Bachelor thesis

in Physics

submitted by

Selina Karin Gaisser

born in Speyer

2022

Cryogenic MCP detector performance benchmarking at the CSR

This Bachelor thesis has been carried out by Selina Karin Gaisser

at the

Max-Planck-Institut für Kernphysik in Heidelberg

under the supervision of

Dr. Holger Kreckel

and

Dr. Oldřich Novotný

Benchmarking der Leistung kryogener MCP-Detektoren im CSR-Speicherring:

Molekulare Fragmentierungsprozesse können mit Hilfe spezieller Detektionssysteme sehr genau beobachtet werden. Das MPIK in Heidelberg betreibt einen solchen Detektor mit dem 3D-Bildgebungs-Detektor am kryogenen Speicherring CSR. Hier werden vor allem Reaktionsprodukte aus Dissoziativer Rekombination DR von Molekülionen mit Elektronen gemessen und beobachtet. Um zuverlässige Messergebnisse zu erhalten, muss die Einstellung des Detektors sorgfältig an die jeweilige Umgebung und die Umstände des Experiments angepasst werden. Zu diesem Zweck wurde der Detektor in dieser Arbeit auf die optimale Konfiguration im vorgesehenen Betriebsmodus untersucht. Zusätzlich zu diesen Untersuchungen wird ein neuer Betriebsmodus des Detektors implementiert und auf seine optimalen Parameter hin untersucht. Dieser Modus soll eingeführt werden, um die bisherige maximale Zählrate von $2 \times 10^3 \, \mathrm{s}^{-1}$ zu erhöhen, ohne die gewonnenen Daten zu verfälschen oder eine mögliche Beschädigung des Detektors zu befürchten. Um dies zu erreichen, wird der Detektor periodisch ein- und ausgeschaltet, so dass Sättigungseffekte unter Kontrolle gehalten werden. Hierbei wurden zwei Formeln aufgestellt, mit denen optimale Messergebnisse für die jeweiligen Einstellungen in diesem Modus erreicht werden können. Dabei kommt es auf ebenfalls auf die technischen Möglichkeiten an. Der neue Betriebsmodus wurde bereits mit Zählraten von $\sim 100 \times 10^3 \, \mathrm{s}^{-1}$ erfolgreich angewendet.

Cryogenic MCP detector performance benchmarking at the CSR storage ring:

Molecular fragmentation processes can be observed very precisely with the help of dedicated detection systems. The MPIK in Heidelberg operates such a detector with the 3D imaging detector at the cryogenic storage ring CSR. Mainly reaction products from dissociative recombination of molecular ions with electrons are measured and observed here. In order to obtain reliable measurement results, the setting of the detector must be carefully adapted to the respective environment and circumstances of the experiment. For this purpose, the detector was examined in this work for the optimal configuration in the intended operating mode. In addition to these investigations, a new operating mode of the detector is implemented and investigated for its optimal parameters. This mode is to be introduced in order to raise the previous maximum count rate of $2 \times 10^3 \, \mathrm{s}^{-1}$ without distorting the acquired data or fearing of possible damage to the detector. To achieve this, the detector is switched on and off periodically so that saturation effects are kept under control. Here two formulas were established, with which the settings for optimal measurement results in this mode can be achieved. At the same time, depending on the technical possibilities. The new operation mode at $\sim 10^5 \, \mathrm{s}^{-1}$ was successfully demonstrated.

Contents

II Appendix   55

III Appendix   63

1 Introduction

For thousands of years, humanity has been fascinated by the earth surrounding space and distant stars. Thus, the mystery of space was gradually explored, first by observing the movements of the planets, which gave rise to the first calendars, through the discovery of Kepler's Law, to the first theories about the origin and composition of the universe. Finally, in 1957, humankind set the first step into unknown space with its first satellite [1]. Since then, the universe was explored in giant steps. However, many observed phenomena, e.g., interstellar clouds, are still out of direct reach even with the modern spacecrafts.

Nevertheless, to unravel the mysteries, scientists have developed experimental setups that simulate the harsh conditions in space to understand the interstellar medium.

One such setup is the electrostatic Cryognic Storage Ring (CSR) at Max Planck Institut für Kernphysik (MPIK) in Heidelberg [2]. With temperatures below $6\,\mathrm{K}$ and pressures below $10^{-14}\,\mathrm{mbar}$, the CSR achieves optimal conditions to investigate, e.g., gas-phase reactions of molecules in the interstellar medium [3], which regulate the abundances of the various molecules.

In interstellar clouds, an essential gas-phase reaction is Dissociative Recombination (DR), a neutralization process for positively charged molecular ions [4]. In this process, an electron recombines with the positively charged molecule, which then decays into its neutral atomic or molecular fragments:

$$\mathrm{AB^+ + e^- \longrightarrow A + B.} \tag{1.1}$$

To observe such fragmentation processes in the CSR the resulting neutrals must be detected reliably, so that not only the rate of such events but also the relative geometry of the fragments can be determined [5]. Thus, the 3D-imaging detector NICE was developed and implemented [6]. With the combination of a MCP, a phosphor screen anode, and a high-speed CMOS camera, the detector has imaging and timing abilities for a fragment impact rates up to about $2 \times 10^3\,\mathrm{s^{-1}}$, the maximum count rate.

The first goal of the work presented in this thesis was to characterize the NICE detector and optimize the operation parameters for future experiments. Even though the detector was already used for several CSR experiments in the past, the experimental conditions evolved and new, dedicated detector characterization was needed.

The second goal was to increase the maximum count rate. To this end, a new mode of operation, called *fast switching*, was implemented, tested, and characterized.

With these goals in mind, measurements were performed with various settings for both operation modes.

Outline of this work

The introduction of this work is followed by a brief description of the CSR in chapter 2, with a special emphasis on the NICE detector.

Chapter 3 explains and presents the measurement schemes for the detector characterization, the data analysis and a short interpretation of the individual set of results. The chapter is divided into four sections. The first section shortly explains what kind of measurements were taken. The second one demonstrates the analysis on one reference data set. After the measurements to optimize the standard mode are discussed. Last, the switching mode is implemented, tested and optimized.

The last two chapters draw a conclusion (chapter 4) and give a short outlook for the possible future upgrades of the CSR detection system (chapter 5).

2 Experimental setup

This chapter gives a brief overview over the CSR and the NICE detector. Hereby, the important characteristics of the CSR are described, a more detailed description is given by Hahn et al. [2]. The description of the NICE detector is more detailed, due to its importance for this work.

2.1 The Cryognic Storage Ring (CSR)

The electrostatic Cryognic Storage Ring (CSR) at the Max Planck Institute for Nuclear Physics in Heidelberg is a unique device to study collision and laser interactions of fast atomic, molecular, and cluster ion beams. Due to the electrostatic nature of the CSR, it is able to store ions with kinetic energy range of $20 - 300$ keV per charge, independently of the ion mass. Another advantage of CSR is the cryogenic environment with beamline-chamber temperatures below 6 K. The low temperatures combined with a pressure below 10^{-14} mbar allow exceptionally low residual-gas densities and therefore suppressed residual-gas scattering, resulting in beam storage lifetimes in the order of 1000 s.

Fig. 2.1 shows a schematic draw of the CSR. It shows the square structure of the ring, with a circumference of 35.12 m. Each of the four straight sections (labeled alphabetically) is equipped with it's own tools and devices for experimental purposes and beam diagnostics.

In each 90° corner there are two pairs of 6° and 39° deflectors and two quadrupoles to redirect and focus the beam.

Taking the CSR scheme in Figure 2.1 as reference, the beam is injected at the upper left corner between section **A** and **D**, following section **A** in a counter-clockwise direction.

A is a merged neutral beam section, with an Radio Frequency (RF) bunching system.

In section **B** the electron cooler provides a merged electron beam for electron cooling or as a collision target. Downstream of this interaction zone the Cold Movable Particle Counter (COMPACT) and NICE detectors are positioned. NICE is implemented behind a 6°, so that only neutral fragments can hit the surface since all other charged particles are deflected.

The next section **C** is for diagnostic purpose. Here, current and Schottky pickups are implemented.

With two implemented position pickups, the last section **D** also includes tools for beam diagnostics.
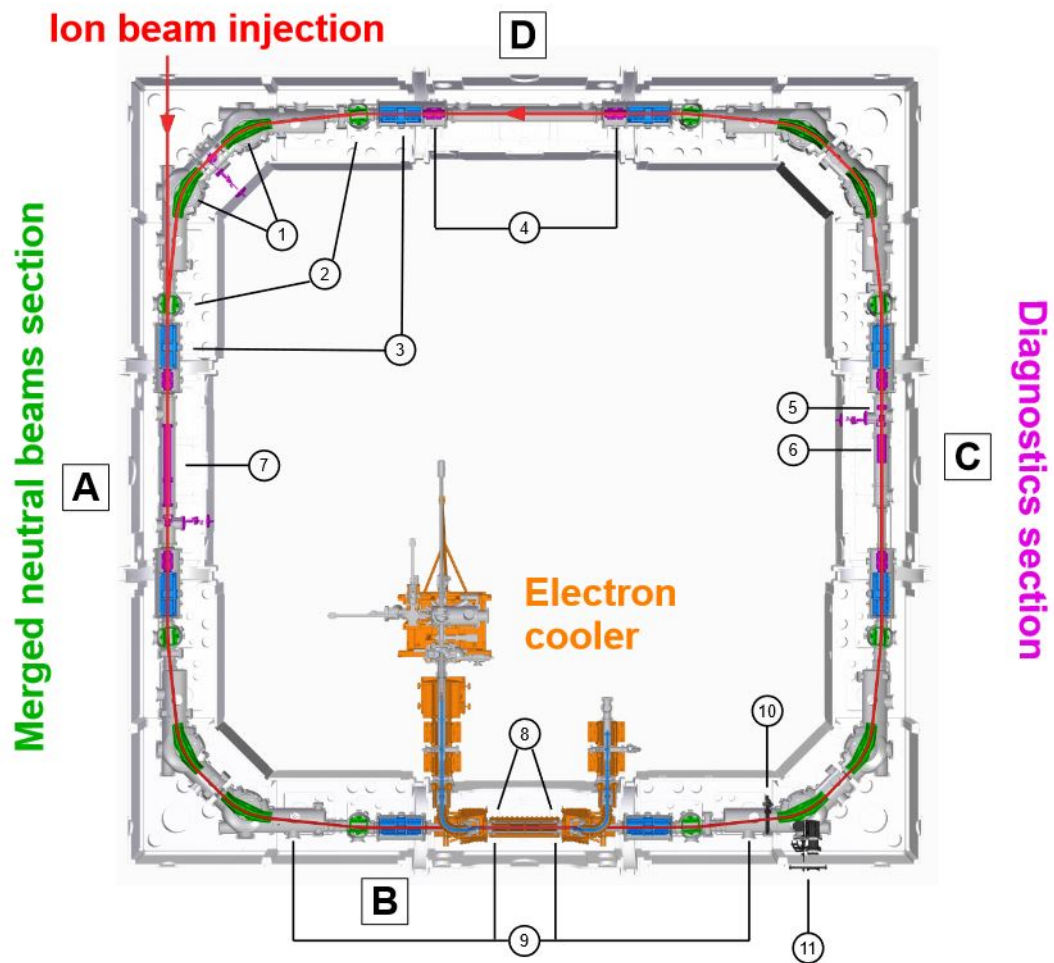
Figure 2.1: Schematic setup of CSR. The ion beam is injected in the corner between sections **D** and **A** and follows the tube counterclockwise. Two 39° (1) and 6° (2) deflectors redirect the beam on each 90° corner (green). Two quadrupole doublets (3) enclose the deflectors to focus the beam before and after redirection. The position (4), current (5), Schottky pickups (6), and the RF bunching system (7) are diagnostic instruments (purple). Located in section B is the electron cooler (8). Next to the electron cooler are the viewport positions for laser experiments (9). At the end of section B are the COMPACT (10) and NICE (11) detectors. Adopted from [7].

2.2 Neutral Imaging in Cold Environment (NICE)

The Neutral Imaging in Cold Environment (NICE) detector was implemented after the merged-beams section to observe fragmentation processes, e.g., the previously discussed DR processes. The development and construction of NICE are described in detail by A. Becker [6]. This section describes the detector's structure and operating principles and concentrates on the essential aspects in the context of this thesis.

2.2.1 Overview

Figure 2.2 shows an illustration of the NICE detector. The neutral fragments first hit the surface of a MCP. There, each particle triggers an electron avalanche within the MCP. Afterwards, the electrons are accelerated towards a phosphor screen, which functions as an anode. The electrons induce light spots and simultaneously a current pulse on the conductive layer of the screen. A digitizer records the electronic pulses from the phosphor screen, whereas a mirror guides the generated photons outside of the cryogenic environment, where a fast CMOS camera captures them. Both systems together record timing and positioning, but independently. The later introduced COBRA principle is necessary to correlate both parameters.

In the following, the *imaging data* refer to gathered camera data, and the *electronic data* refers to those from the digitizer.
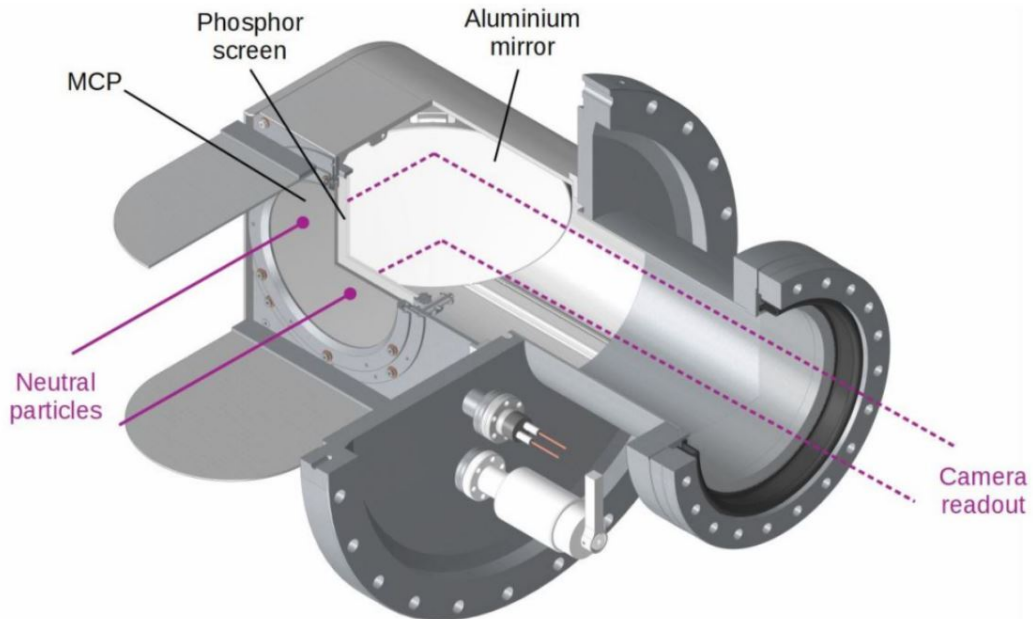

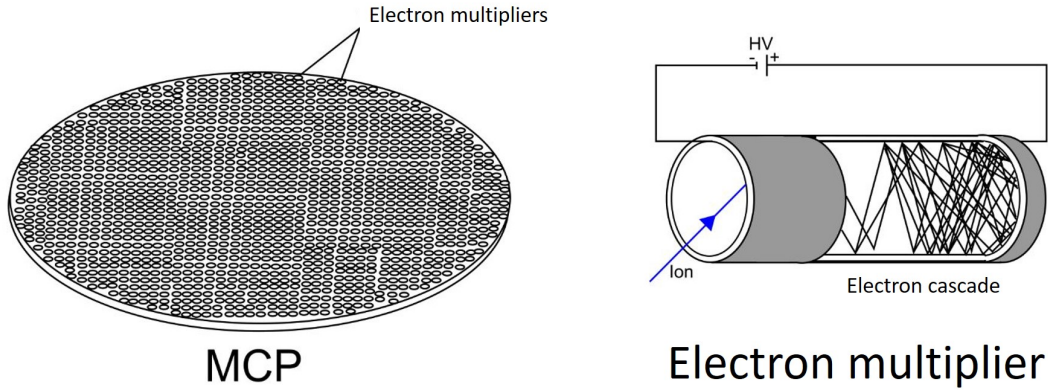Figure 2.2: Scheme of the NICE detector. Adopted from [5].

Figure 2.3: Model of an MCP. Left: A single MCP plate with lots of electron multiplier micro channels. Right: An illustration of the operating principle of a single electron multiplier channel. Adopted from [8].

2.2.2 Microchannel Plate (MCP)

A Microchannel Plate (MCP) is a specific electron multiplier for detecting, e.g., electrons, ions, or fast neutral particles. It consists of a high electric resistance plate (e.g., lead glass), which contains thin, parallel, slightly inclined, channels coated with semiconductor material (see Fig. 2.3 left scheme). A particle hit in one of these channels triggers an avalanche of electrons (see Fig. 2.3 right scheme). As a result, the electrons within the material are depleted and have to be replenished. The time for the electron replenishment depends on the bias voltage between the MCPs front and back and on the impedance of the MCP material.

Typical signal amplification for a single MCP is in the range of $10^3 - 10^4$. This amplification is, however, most times, not sufficient. Therefore two MCP plates are connected in series, whereby the second plate is 180° rotated, e.g., Fig. 2.4. This configuration is called Chevron configuration and reaches amplifications of up to 10^7 at room temperature conditions. [9]

This work uses an MCP in Chevron configuration from PHOTONIS. The active area of the round MCPs has a diameter of 120 mm. Both MCP plates are 1.5 mm thick. Each channel has a diameter of $25\,\mu$m with an angle of 8°. Due to the semiconductive nature of the MCP base material, the resistance increases with decreasing temperatures. While at room temperature the NICE-MCP impedance is about $4\,\text{M}\Omega$, for 6 K it increases to several $10\,\text{T}\Omega$. That, in turn, increases the recharge time of each channel. To keep this recharge time at an acceptable level, the MCP must be heated to $\sim 40\,\text{K}$, which results in a resistance of $\sim 2\,\text{G}\Omega$ with a detector efficiency limited dominantly by the pore-opening area fraction of $\sim 60\,\%$ (open area ratio).

For proper operation the two faces of the MCP-stack (front and back) are kept at different voltages with respect to ground potential, i.e., U_{MCP_f} and U_{MCP_b}. The MCP bias voltage $U_{\text{MCP}_\text{bias}}$ refers to the difference between the two voltages, i.e., the

full acceleration voltage within the Chevron stack.

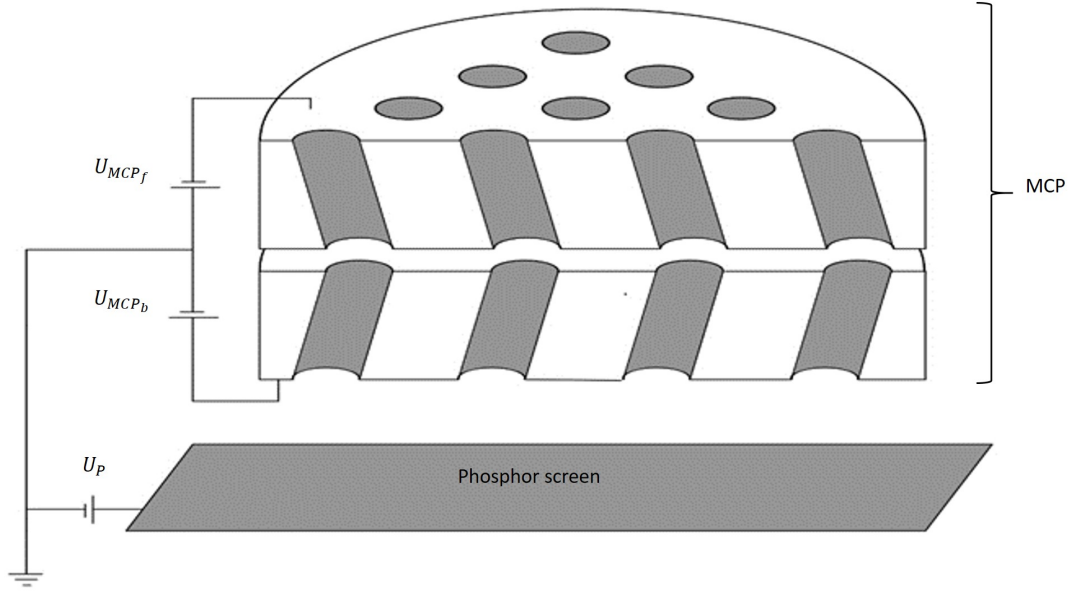

Figure 2.4: Scheme of a MCP Chevron configuration with a phosphor screen anode.

Dead time

Each electron cascade depletes the electrons in the MCP channel walls. Thus, the walls have to replenish the lost electrons. This recharging process needs time. If an exponential recharging process is assumed, a characteristic time constant τ can be calculated as [10]:

$$\tau = \kappa R_{\mathrm{Ch}} C_{\mathrm{Ch}} = \kappa R_{\mathrm{MCP}} C_{\mathrm{MCP}}. \tag{2.1}$$

Here R_{Ch} and R_{MCP} are the resistances, C_{Ch} and C_{MCP} the capacities of the single channel and the whole MCP stack (front and back MCP), respectively, and κ is a constant, which characterizes an unspecific recharge circuit.

In order to calculate the recharging time for the implemented MCP, a model of a parallel plate capacitor was presumed [11]:

$$C_{\mathrm{MCP}} = \frac{\epsilon_0 \epsilon_r A}{d}. \tag{2.2}$$

ϵ_0 is hereby the vacuum permittivity, ϵ_r the dielectric permittivity, A the detector surface area and d the thickness of the MCP. In Tab. D.1 are the specifications for the detector. Given the open area ratio of the MCP of $\sim 60\,\%$ and the fact that the open area is vacuum ($\epsilon_r = 1$), an effective dielectric permittivity of $\epsilon_{r,eff} =$

$0.4 \cdot 8.3 + 0.6 \cdot 1$ can be assumed. It follows:

$$C_{\mathrm{MCP}} = \frac{8.85 \times 10^{-12}\,\mathrm{F\,m^{-1}}\,(0.4 \cdot 8.3 + 0.6 \cdot 1)\left(\frac{120 \times 10^{-3}\,\mathrm{m}}{2}\right)^2 \pi}{1.5 \times 10^{-3}\,\mathrm{m}} \tag{2.3}$$
$$\approx 260\,\mathrm{pF}.$$

Most of the charge is assumed to be depleted within the last $20\,\%$ of the channel length in the back MCP only due to the exponential nature of the avalanche process [11]. That is, these $10\,\%$ of the MCP stack determine the effective capacity of $C_{\mathrm{MCP}}^{\mathrm{eff}} = 26\,\mathrm{pF}$. The resistance of $R_{\mathrm{MCP}} \approx 1.96\,\mathrm{G\Omega}$ for the full stack was determined from the $\sim 1\,\mu\mathrm{A}$ bias current at $\sim 1778\,\mathrm{V}$ bias voltage and $\sim 40\,\mathrm{K}$ detector temperature. For one MCP-plate, the resistance should be $R_{\mathrm{MCP}} \approx 0.98$

Thus, the characteristic recharge-time constant is:

$$\tau \approx 26\,\mathrm{pF} \cdot 0.98\,\mathrm{G\Omega} = 25.48\,\mathrm{ms}. \tag{2.4}$$

For the recharging constant, we assume $\kappa = 1$. The given time is assumed for only one channel. Thus, to compare the time with the gathered data, further calculation are necessary.

2.2.3 Phosphor screen and readout signals

The electron cloud generated by the MCP is accelerated further electrostatically and hits a phosphor screen anode. The impinging electrons initiate two different processes, which lead to an optical and electrical signal.

By hitting the phosphor screen, the electron clouds induce fast-decaying light spots on the phosphor screen. These light spots are then captured by a high-speed Complementary Metal-Oxide Semiconductor (CMOS)-camera, which provides the optical signal.

To act as anode, a voltage on the orders of kV is applied to the phosphor screen. Now, the negative charged electrons induce a ns-short current pulse on the conductive layer of the surface of the phosphor screen. A directly to the phosphor screen connected electronic signal decoupling circuit separates the pulse, which is further multiplied by an amplifier. Finally, a digitizer records the pulses. Those are used to determine the corresponding pulse-heights and pulse-times. The pulse height distribution shape depends on the MCP supply voltage as shown in Fig. 2.5.

NICE uses a phosphor screen provided by German Imaging Detector Solutions (GIDS). P47 was chosen as the phosphorescent material due to its fast decay time of $\sim 100\,\mathrm{ns}$ from $90\,\%$ to $10\,\%$ of its peak intensity. A $50\,\mathrm{nm}$-thin aluminum layer provides the conductive layer [12].

For this thesis, a Standford Research SR445 amplifier with an $50\,\Omega$ input impedance was implemented to amplify the electronic signal. The gain was fixed for each stage to about a factor of five. In the measurements either one or two amplification amplifications were used.

The produced photons are guided outside of the cryogenic environment with an aluminium mirror. A high-speed CMOS-camera records the photons. The camera system has a resolution of 512×512 pixels with a size of $14 \times 14\,\mu$m each and a frame-readout rate of $\sim 1\,$kHz.
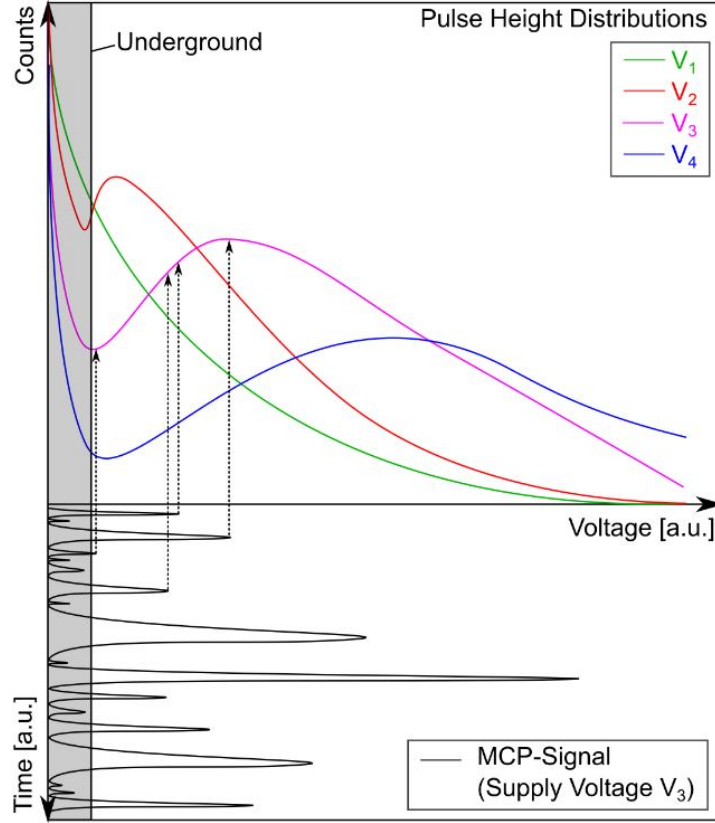

Figure 2.5: Electrical signal acquisition for four different supply voltages, whereas $V_1 < V_2 < V_3 < V_4$. The blue curve is near the saturation point. Adopted from measurements with another MCP detector. Adopted from [13].

2.2.4 Data acquisition timing

Additionally to the digitizer and camera readout, the detector is equipped by a single-pixel Silicon Photomultiplier (SiPM). This is used to provide a sensitive position-insensitive trigger signal from the photons of the phosphor screen. The trigger is then used to post-trigger the digitizer waveform and determine the *number of pulses* N_p, the *arrival time* t_p, the *amplitude* A_p and the pulse-area *integral* I_p, which are stored. Due to the limitation of the maximum acquisition rate, the full waveform is not stored.

In parallel to the electronic signal readout, the SiPM signal triggers the camera. Fig. 2.6 illustrates this process. The camera continuously integrates the incident

photons. If triggered, the camera continues recording for additional $2\,\mu$s. This delay is applied in order to collect all fragments from, e.g., one DR event. Afterwards, the shutter of the camera closes and the data are stored. After $50\,\mu$s without a triggered event, the camera shutter is shortly closed without storing the data and then new acquisition is started. This procedure avoids extensive collection of noise. For each stored camera frame an online analysis software obtains the *number of spots N_s* and for each one the *amplitude A_s*, the *integral I_s* and the *pixel-positions x_s and y_s*. [5][7]
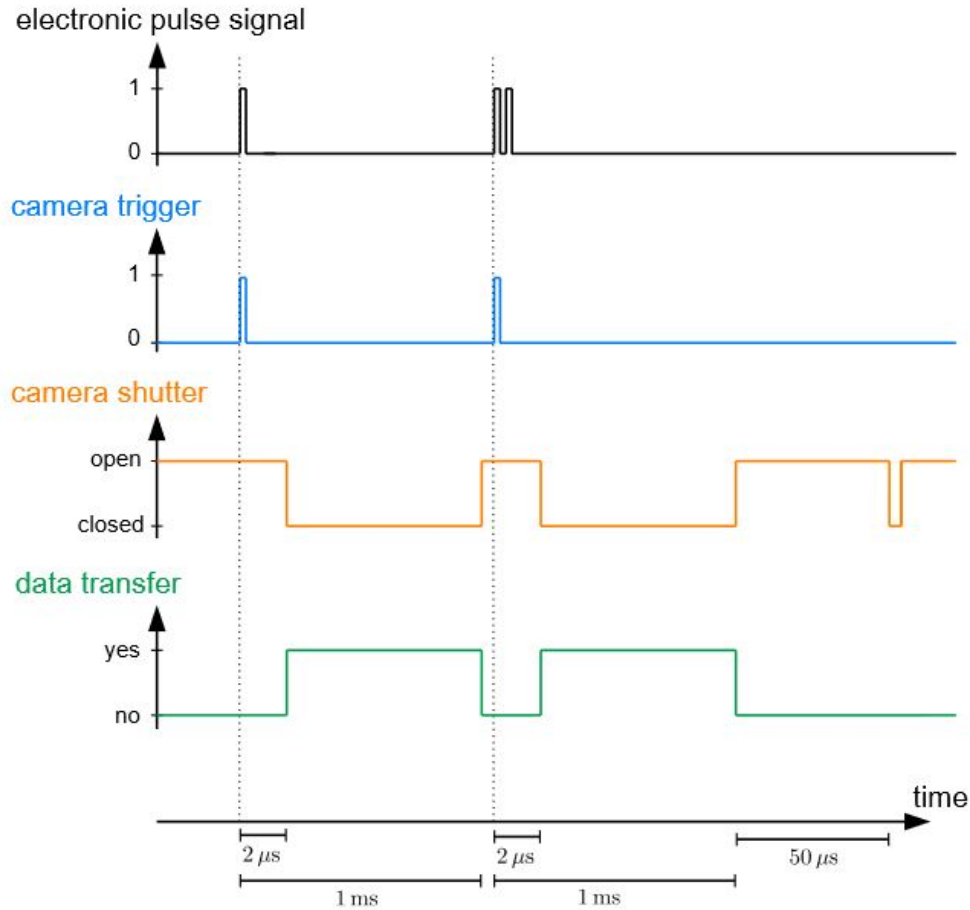

Figure 2.6: Scheme of the data acquisition timing of the NICE detector - simplified and not to scale. The start of an event is indicated by the vertical dotted lines. Adopted from [7].

2.2.5 Correlation of Spot Brightness and Pulse Amplitude (COBRA)

In order to retrieve a 3D image of the fragmentation process, timing and positions have to be known jointly. As explained above, the camera documents the positioning,

15

and the digitizer records the timing. Hence, the system records both parameters independently. To correlate both required parameters, Urbain et al. developed a new acquisition scheme [14]. The developed scheme is called COBRA principle. Further information is given in section 3.2.

2.2.6 Operating mode

Each measurement starts with the beam injection and ends after a defined time period. This period is called the injection-cycle duration, the time after the ion-injection in the ring is called the *storage time t*. Multiple injection cycles are repeated within one measurement run, where no other parameters are changed. The measurement itself will be with two different operation modes.

The *standard mode*, once started, continuously measures until the end of the injection cycle. This mode is suitable for a count rate up to $2\,\mathrm{kHz}$. Above this value, the MCP can be saturated, which could lead distortion of the data or even damages in the detection system.

Thus, the new *switching mode* was developed. Instead of measuring continuously, a power supply switches the MCP bias voltage on and off with a defined frequency and duty cycle during the measurement time. Here higher impact rates are allowed because the detector can recover in the off-periods.

It is important to know the optimal parameter settings for both operating modes. These are for the standard mode the MCP *front $U_{\mathrm{MCP_f}}$* and *back $U_{\mathrm{MCP_b}}$ voltages*, as well as the *phosphor screen voltage U_{P}*. Besides these three parameter settings, the switching mode has two more options: the switching *frequency f* and the *duty cycle d* , indicating the fractional time where the detector stays on. For more details see section C.1.

3 Measurements

In order to gain a better understanding and to optimize the detector operation a parameter sweep was performed. Settings such as beam intensity and voltages were varied. In addition, the behavior of the detector during a switching operation was investigated. In particular, we have investigated how the recovery time of the detector varies, how the short detection times affect the behavior of the detector, when the detector enters saturation, and the influence of the different voltage parameters.

This chapter starts first withe the introduction of which fragmentation process is to expected in this measurement series.

After, a reference data set were analyzed, the single measured data presented and explained.

The reference data analysis follows the measurements with the standard operation mode of the detector. Each parameter sweep is explained, the analysis and observation clarified and interpreted.

At least, the performing of detector switching is discussed. In a first step, the depletion and recovery time of the detector was investigated. Secondly, the short measurement times were valued, followed by the discussion of the count rates. At least, one measurement with CF^+ in the switching mode is presented.

The measurements were carried out at the CSR at MPIK in Heidelberg in fall 2021 and the re-measurements in winter 2022.

List of analysis parameters

t Storage time
N_s Spot number
N_p Electronic pulse number
A_s Spot amplitude
A_p Pulse height amplitude
I_s Spot integral
I_p Pulse height integral
Δt_d Time difference of electronic doubles
σ_{corr} Correlation Spread
t_{ref} Reference time
t_{ref}^{on} Detector on time of the reference time

3.1 Fragmentation process

For detector optimization, it was decided to perform the measurements with a beam as stable as possible to obtain a stable impact rate of neutral fragments. Thus, the measured neutralization process was chosen as collisions of residual-gas with molecular cations from the stored beam.

Two main collision processes are assumed. O_2^+ was chosen to perform the test, due to its similar structure.

In the first process, an residual gas molecule Y collides with a molecular cation AB^+ of the stored beam and decays into its single components of $A + B^+$ or vice versa: [15]

$$AB^+ + Y \longrightarrow A + B^+ + Y \tag{3.1}$$

This process occurs because the collision energy corresponding to the kinetic energy of AB^+ (ABkeV) is strong enough to break the bond between the diatomic molecule. The second process is an electron capture process. The residual-gas molecule Y collides with the molecular cation AB^+. Here, Y captures an electron from AB^+. The collision energy also leads to a dissociation of the molecule into its atomic components [6], [16]:

$$AB^+ + Y \longrightarrow A + B + Y^+. \tag{3.2}$$

3.2 Analysis of a reference data set

This section will guide through the process of how the data was taken, analyzed and interpreted.

Therefore, a reference data set was analyzed as an example. The following list gives the parameter settings, where all voltages are with respect to ground potential:

- MCP front voltage: $U_{\mathrm{MCP_f}} = -778\,\mathrm{V}$

- MCP back voltage: $U_{\mathrm{MCP_b}} = 1000\,\mathrm{V}$

- Phosphor screen voltage: $U_{\mathrm{P}} = 11\,000\,\mathrm{V}$

- Maximum impact rate: $4\,\mathrm{kHz}$

- Injection cycle duration: $t = 50\,\mathrm{s}$

- Beam on time: $t_{\mathrm{on}} = 40\,\mathrm{s}$

- Beam off time: $t_{\mathrm{off}} = 10\,\mathrm{s}$

- Temperature: $T = 40\,\mathrm{K}$

In order to gather the electronic data, the electronic pulse was amplified with the SR445 amplifier, mentioned in Sec. 2.2. Besides, a two amplification stage, with each five times was chosen.

Runs

A run consists of data acquisition over multiple ion beam injections for one specific detector parameter setting. However, not all of the gathered data have the same statistical quality. The number of recorded events (see Sec. 2.2) differs from run to run. Hence, all distributions in this chapter are normalized to their integral for the plots, except for the 2D-imaging plots. I.e., every bin entry, also called count, is divided by the total amount of recorded entries.

Count rate

Especially for the second goal of this thesis to counteract the issue of the limited event detection (see Chap. 1), it is crucial to know the recorded count rate. In order to obtain a general view of count rate evolution with ion beam storage time, a count rate plot was created, shown in Fig. 3.1a. The count rate is the rate of events per second on the detector. A count rate plot consists of the average number of detected events per second as a function of the storage time, averaged over all injection cycles. In the example of Fig. 3.1a, the first $40\,\mathrm{s}$ show the count rate for the beam-on time with a count rate of $\sim 500\,\mathrm{s}^{-1}$. After that, the count rate drops significantly to $\sim 90\,\mathrm{s}^{-1}$. Here, the beam was kicked out of CSR by removing the voltage of one 6 degree deflectors (see Fig. 2.1). The remaining measured counts are due to dark counts, further discussed in Sec. 3.3.4.

Event multiplicity

Not just one but multiple fragments could be measured in one event. The data acquisition systems can assign any number of spots detected with the camera N_{s} and electronic pulses N_{p} evaluated with a digitizer for each triggered event, given in Fig. 3.1 (b) and (c), respectively. This assignment is essential for some data sets, where it is better to filter on one or two detected fragments instead of all. This is the case, for example, for measurements where just one fragment is expected.

2D-imaging plots

As mentioned in Sec. 2.2, NICE acquires positioning data $(x_{\mathrm{s}}, y_{\mathrm{s}})$ from the camera. A plot showing the integrated camera spot positions, called 2D-imaging plot, is suitable for examining this. Fig. 3.2 shows such a plot, where the round shape of the distribution is due to the round MCP aperture. At horizontal position $275\,\mathrm{px}$ and vertical position $280\,\mathrm{px}$ a peak is visible. This peak represents the oxygen fragments resulting from the collision of $O_2{}^+$ with residual gas, described in the Sec 3.1. The fact that the detector surface is completely filled towards the outside is due to detected dark counts.
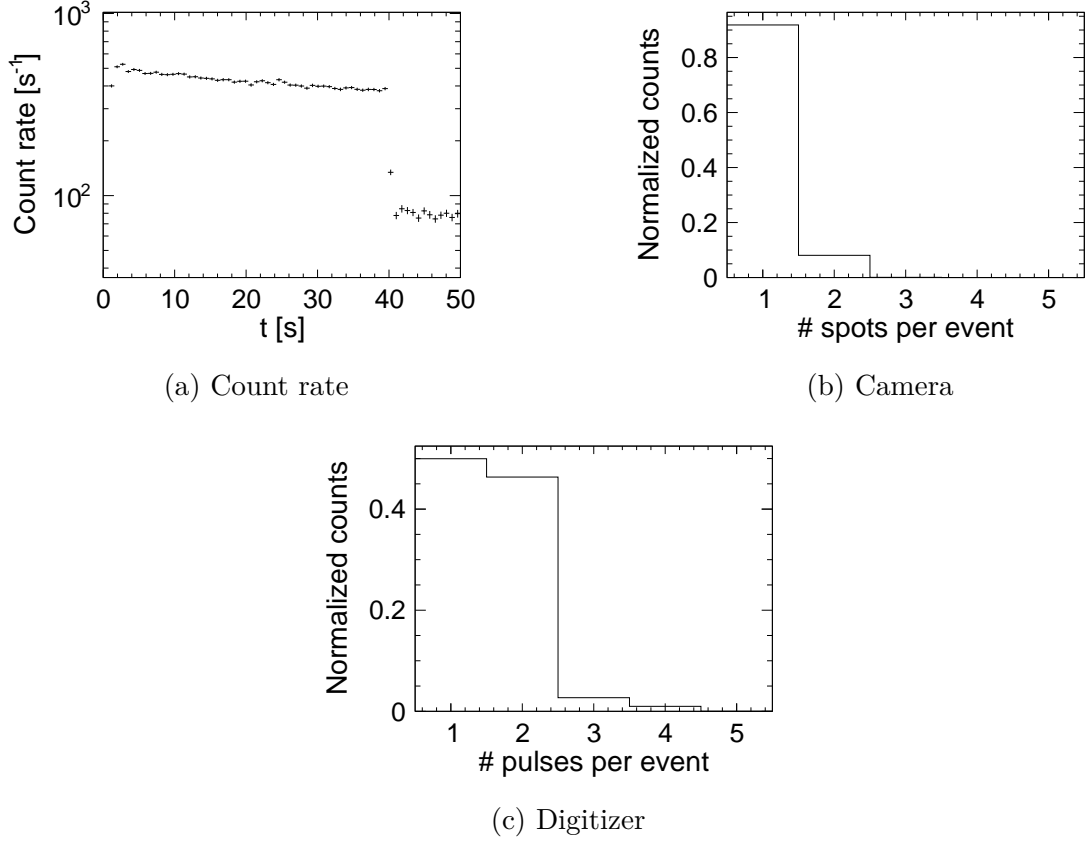
(a) Count rate

(b) Camera

(c) Digitizer

Figure 3.1: The detected (a) count rate and the recorded fragments per event for the triggered (b) camera (N_s) and (c) digitizer (N_p).

Spot amplitude A_s

Besides the impact position data, the camera also records the highest amplitude detected in a single pixel for each spot (A_s). Fig. 3.3 (a) shows a plot of this recorded signal. The distribution shows one peak, at $\sim 100\,\text{arb.u.}$, and a tail on the left side. However, the tail of the distribution is due to the dark counts.

Pulse height A_p

Additionally to the camera data, the data obtained with the digitizer are also relevant. Fig. 3.3 (b) shows a pulse height distribution. It shows a high, sharp peak at $\sim -0.1\,\text{V}$ mostly due to electronic noise. Another broad peak is visible at $\sim -0.55\,\text{V}$. This peak indicates the real events from $O_2{}^+$ fragments in collisions with residual gas. Therefore, it is clearly visible. Around $-0.95\,\text{V}$, there is one single noticeable bin. Below this value, the digitizer cannot record any lower voltages. Thus, all counts below this value are summed up in this bin, so it is not essential for the later analysis.

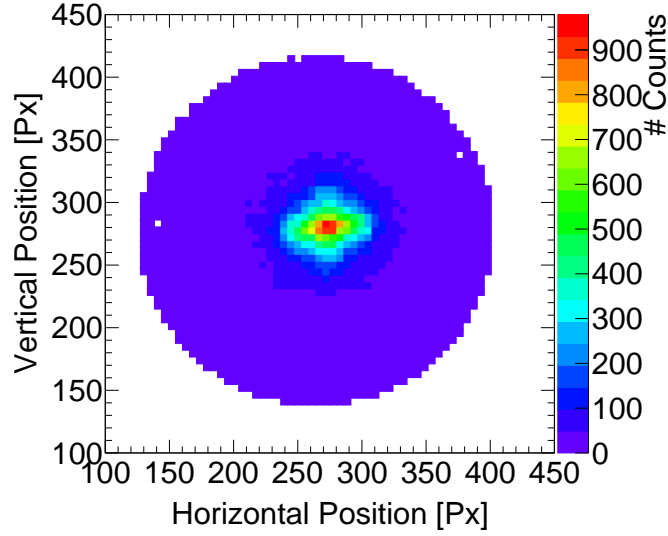The values of the pulse height are negative. This is due to the negative voltage

Figure 3.2: 2D-Imaging.

pulse induced by the electron avalanches. They can be converted into positive values, as later done in the COBRA analysis.
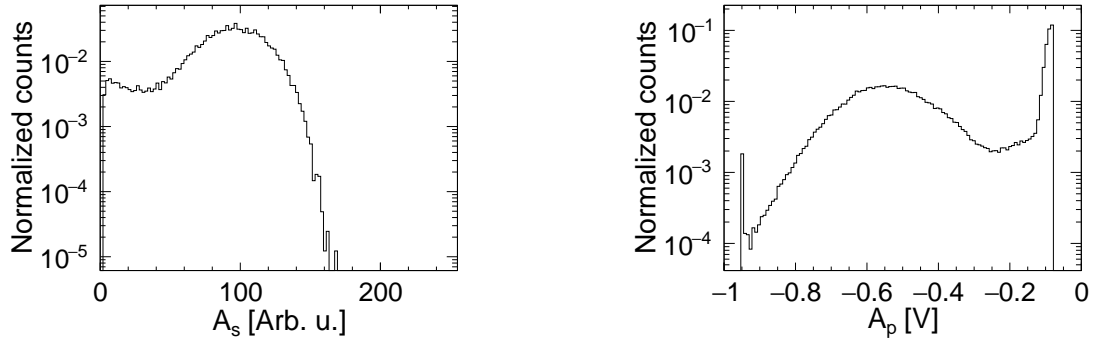
Time difference of electronic doubles Δt_d

Another essential distribution is based on the time difference Δt_d between two pulses in the same event (electronic doubles). For the plot in Fig. 3.3 (c), the recorded time of each second fragment hit gets subtracted from the first one in the same event. The high peak at the beginning of the spectra indicates that most doubles from $O_2{}^+$ fragmentation (see Eq. 3.2) occur within a short time interval. After that, only occasional single random coincidences are visible.

### Storage time evolution plots

For some evaluations, it is helpful to visualize the evolution of a certain distribution with the ion beam storage time t. Two examples of that are the spot amplitude and pulse height distribution evolution with the storage time, e.g., Fig. 3.4 (a) and (b). Both plots show a continuous peak at $\sim 100\,\mathrm{arb.u.}$ for the spot amplitude and $\sim -0.55\,\mathrm{V}$ for the pulse height distribution until the beam is removed from CSR. For the beam-off time, no clear peak is visible.

For further investigations, the stable peak in both distributions is investigated. Thus, the vertical slices are taken and fitted with Gaussian distributions resulting, , e.g., for bin ten in means of $A_\mathrm{s}^\mathrm{mean} = (97.3 \pm 0.8)\,\mathrm{arb.u.}$ and $A_\mathrm{p}^\mathrm{mean} = (-0.547 \pm$

(a) Spot amplitude distribution.

(b) Pulse height distribution.
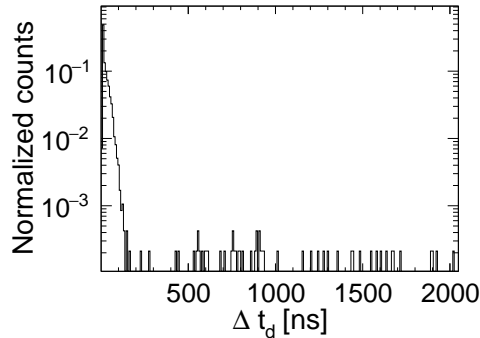
(c) Time difference distribution of electronic doubles.

Figure 3.3: The plots are examples for a typical (a) spot amplitude, (b) pulse height, and (c) electronic doubles time difference distribution.

0.004) V (see Fig. 3.4 (c) and (d)). The various means were then plotted against storage time in Fig. 3.4 (e) and (f).

COBRA

This section briefly introduces the COBRA principle. For more information, see Urbain et. al. [14], Becker [6], or Paul [7], whose described evaluation is followed in this thesis.

COBRA should connect the timing data of the electronic signal with the camera data. Hence, in the first COBRA analysis step, the different amplitudes and integrals of the signals are linked via 2D histograms, i.e., pulse height amplitude A_p against spot amplitude A_s, pulse height amplitude A_p against spot intensity I_s, pulse intensity I_p against spot amplitude A_s and pulse intensity I_p against spot intensity I_s, shown in Fig. 3.5. Similar to the evaluation in [7], the last plot will be used for further analysis. In principle, however, any of these plots can be used for analysis.
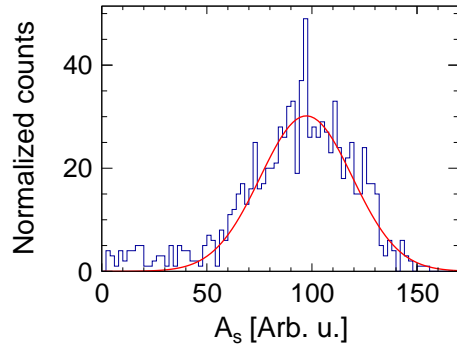
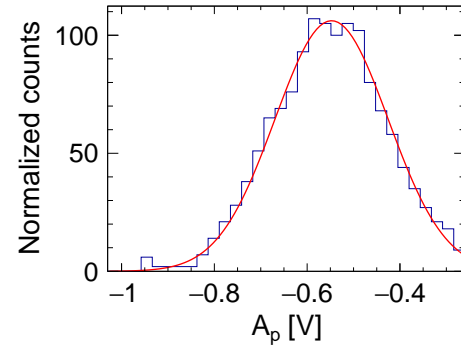In the next step, the plot was split into vertical slices for each spot intensity I_s.
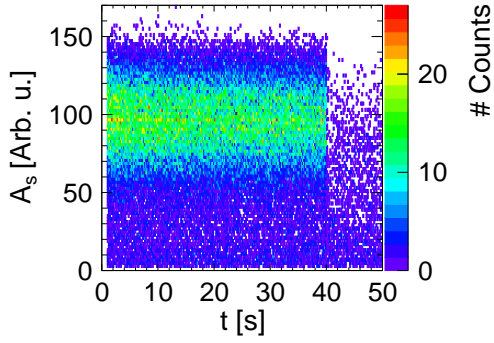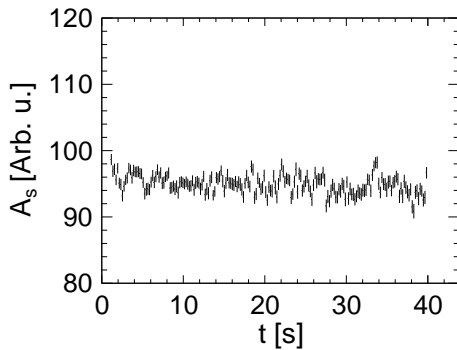
(a) Spot amplitude time evolution plot
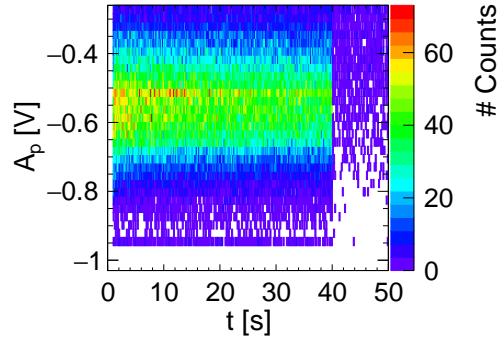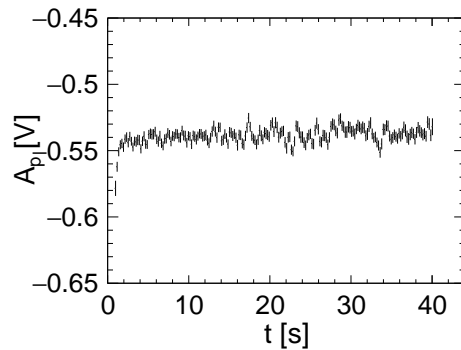

(b) Pulse height time evolution plot

(c) Spot amplitude distribution at slice $t \approx 5\,\text{s}$

(d) Pulse height distribution at slice $t \approx 5\,\text{s}$

(e) Spot amplitude mean vs. storage time

(f) Pulse height amplitude mean vs. storage time

Figure 3.4: Storage time t evolution of the spot amplitude A_s (a) and the pulse height A_p (b) distribution. (c) and (d) show the distribution for one bin with a Gaussian fit. The means and there errors are plottet in (e) and (f) against the time. See text for further explanation of the panels.
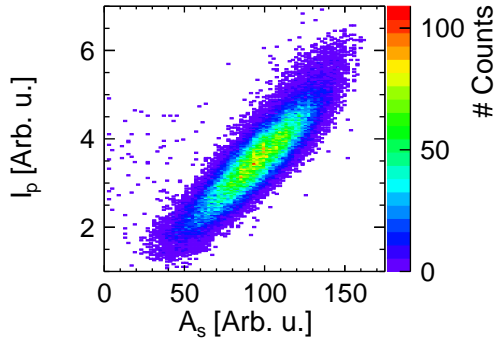
Each slice was analyzed one by one and fitted with a Gaussian distribution. The means and the Gaussian sigma of the fit function then were plotted against spot
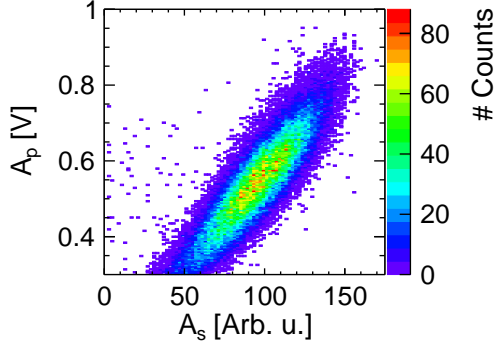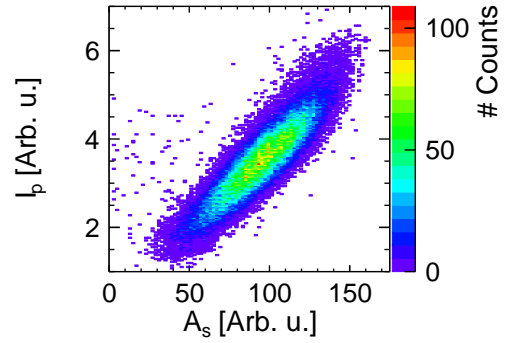
(a) Pulse amplitude against spot amplitude
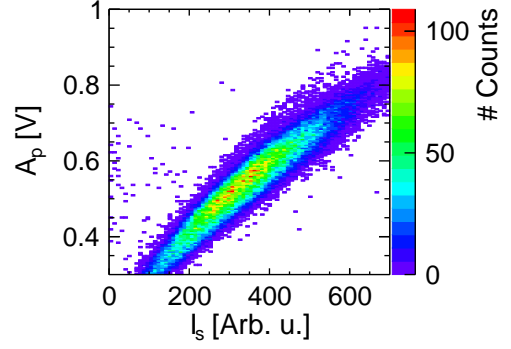
(b) Pulse amplitude against spot intensity

(c) Pulse intensity against spot amplitude

(d) Pulse intensity against spot intensity

Figure 3.5: COBRA evaluation - correlation plots of amplitudes and intensities.

intensity I_s in Fig. 3.6 (a). The resulting points were fitted with a polynomial of the sixth degree.

With these fit function, the pulse intensity for each event was assigned to a new calculated spot intensity value, the transformed spot intensity $I_\mathrm{s}^\mathrm{trans}$, shown in Fig. 3.6 (c).

This new plot as rotated by 45° in Fig. 3.6 (b). The axis of the plot are now called correlation spread $\sigma_\mathrm{corr}^\mathrm{spread}$ and correlation axis $\sigma_\mathrm{corr}^\mathrm{axis}$.

At last, Fig 3.6 (b) was projected onto the x-axis to obtain Fig. 3.6 (d). This plot was then fitted with another Gaussian fit. The standard deviation of this fit gives the acceptance level σ_acc of the transformed plot, see Fig. 3.6 (d).

With this acceptance level σ_acc it is important to categorize the received doubles in each run. Thereby, they can be classified in the three following ways:

- invalid: $\sigma_{1,i} > \sigma_\mathrm{acc}$ or $\sigma_{2,i} > \sigma_\mathrm{acc}$ for all combinations of i.

- valid: $\sigma_{1,i} \leq \sigma_\mathrm{acc}$ and $\sigma_{2,i} \leq \sigma_\mathrm{acc}$ for just one combination i.

- ambiguous: $\sigma_{1,i} \geq \sigma_\mathrm{acc}$ and $\sigma_{2,i} \geq \sigma_\mathrm{acc}$ for more than one combination i.

$\sigma_{1,i}$ and $\sigma_{2,i}$ are hereby the positions of the double pair on the correlation axis. Since only valid events can be used for further analysis, the percentage of the valid doubles should be high.

To investigate how good the COBRA performance of the acquired data were, doubles were randomly simulated based on the 2D histogramm plot in Fig. 3.6 (c). Afterwards, it was calculated in which of these categories the doubles belong. For this reference measurement, the results are given in Table 3.1.

invalid [%]	valid [%]	ambiguous [%]
3.9	71.8	24.3

Table 3.1: Results of the COBRA evaluation

(a) Mean values of the vertical slices from Fig. 3.5 (d) fitted by a sixth degree polynomial fit.

(b) As Fig. (c), but rotated by 45°.

(c) Pulse height amplitude against spot intensity.
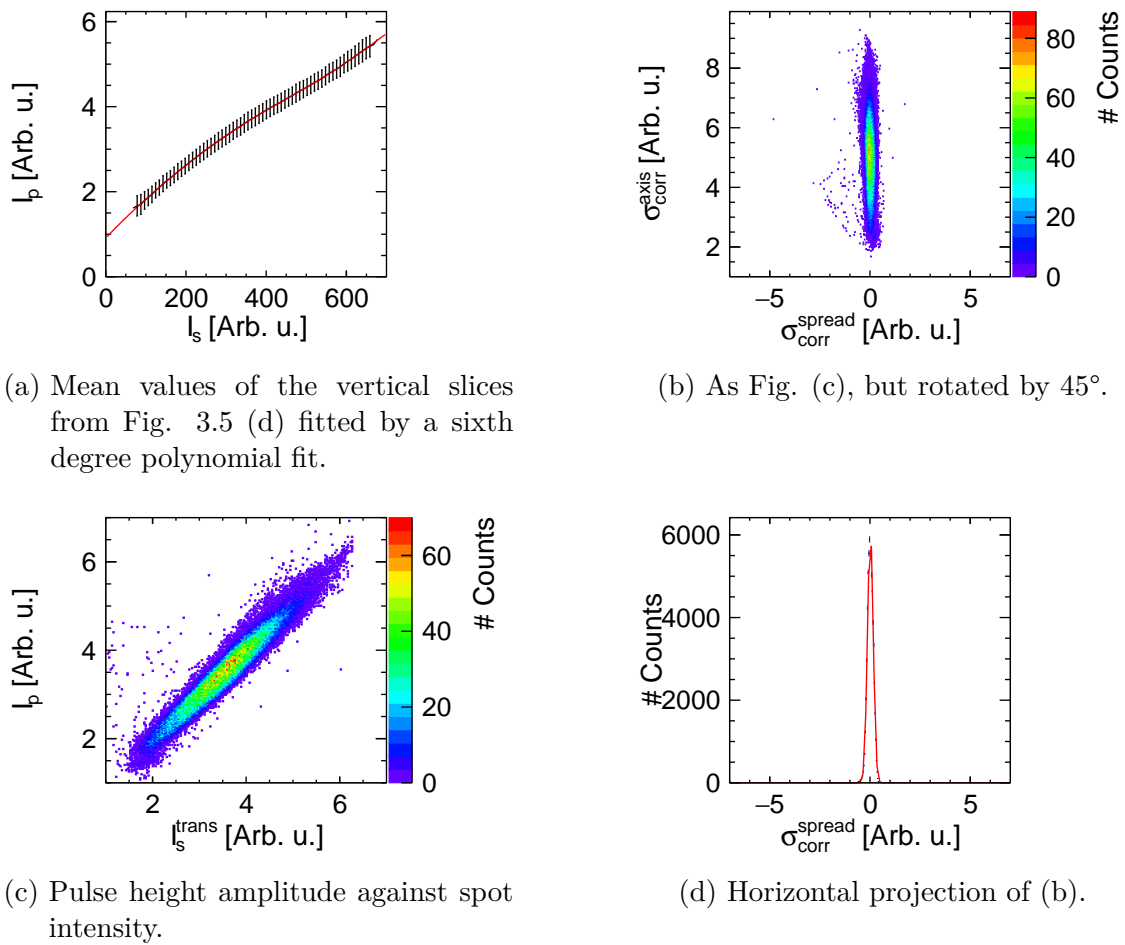
(d) Horizontal projection of (b).

Figure 3.6: COBRA evaluation - transformed data and correlation spread.

3.3 Standard mode

This section describes the part of the measurements to find the ideal voltage settings for future experiments in continuous detection modes.

The measurements were carried out with an SR 445 A amplifier with $50\,\Omega$ input, with two stages, each with an amplification factor of five, as in the previous section. The MCP front $U_{\mathrm{MCP_f}}$, back $U_{\mathrm{MCP_b}}$ and phosphor screen voltages were varied in various setups.

3.3.1 Variation of the Phosphor screen voltage

Measurements

For studying the effects of the accelerating electrons between MCP and the phosphor screen, U_{P} was varied between $3\,\mathrm{kV}$ and $11\,\mathrm{kV}$. The MCP voltages remained constant at $U_{\mathrm{MCP_f}} = -778V$ and $U_{\mathrm{MCP_b}} = 1000V$. The parameters for the individual runs are given in Table D.2.
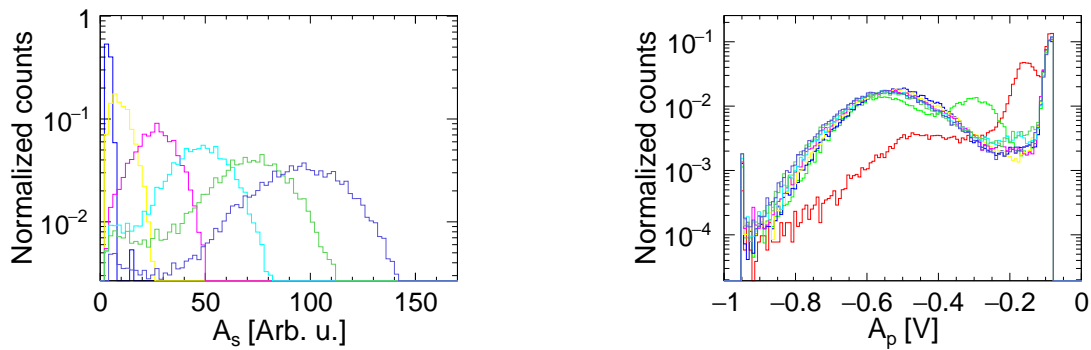

Figure 3.7: Spot amplitude (left) and pulse height (right) distributions for various U_{P}. Black: $3\,\mathrm{kV}$, red: $4\,\mathrm{kV}$, green: $5\,\mathrm{kV}$, blue: $6\,\mathrm{kV}$, yellow: $7\,\mathrm{kV}$, pink: $8\,\mathrm{kV}$, turquoise: $9\,\mathrm{kV}$, dark green: $10\,\mathrm{kV}$, dark blue: $11\,\mathrm{kV}$.

Analysis and observations

Fig. 3.7 shows the different plots of the spot amplitude and pulse height distributions for each run.

Inspecting the spot amplitude, the peak for each distribution shifts towards a lower amplitude with lower voltage, as given in Table 3.2. Similarly, the peaks get narrower. Under a voltage of $U_{\mathrm{P}} = 6\,\mathrm{kV}$, no distribution could be drawn. The last distribution is already so close to $A_{\mathrm{s}} \approx 0\,\mathrm{arb.u.}$, that just a few bins are visible. The pulse height distribution, above $U_{\mathrm{P}} = 7\,\mathrm{kV}$ are comparable with the reference measurement, the lower ones have some irregularities. For $U_{\mathrm{P}} = 3\,\mathrm{kV}$, no

U_P [kV]	6	7	8	9	10	11
$\sim A_s^{\text{Peak}}$ [arb.u.]	0	5	25	50	75	100

Table 3.2: Peak positions for each spot amplitude

distribution could be drawn. The 5 kV distribution has, besides the usual two peaks at -0.55 V and -0.1 V, a third peak at ~ -0.3 V. The 5 kV plot shows no peak around -0.55 arb.u., but one at around -0.45 V can be guessed instead. After that point, the distribution seems to collapse. A previously described third peak is also visible, at -0.15 V.

A COBRA evaluation was performed for a better overview of the combination of the two distributions. Here, the percentage of the valid doubles declines with a lower U_P. The values are given in Table 3.3.

U_P	invalid [%]	valid [%]	ambiguous [%]
11	4.3	71.2	24.5
10	5.1	67.8	27.1
9	4.4	64.7	30.9
8	4.7	59.7	35.6

Table 3.3: Results of the COBRA evaluation.

Interpretation

For both distributions, for phosphor screen values below 7 kV give no or insufficient results. Depending on which data are desired, electric or imaging, two different voltage settings are possible.

To obtain sufficient spot amplitude resolution, a minimum voltage of $U_P = 8$ kV is recommended. Below this voltage, the photon-induced current on the camera sensors is not strong enough to record a clear-shaped distribution. However, the recorded A_s is still on a small scale for $U_P = 8$ kV. With higher U_P, the scales for the peak get bigger. A result of this, are the broader distributions. In the end, one has to decide between a narrower or broader peak.

A minimum $U_P = 6$ kV is necessary for the A_p spectrum. Over that voltage, the distributions do not show any conspicuous deviations. For lower U_P, the spectra-shape changes significantly. These changes are not yet understood. Recording a wave form spectrum would help to investigate that issue. However, concerning the goals of this thesis, the outcome of this investigation would not be within interest.

Nevertheless, to ensure a good COBRA evaluation, the obtained data indicate better results for higher U_P. Thus, future measurement series should measure with the highest possible voltage of $U_P = 11$ kV, above this value a continuous breaktrough current in the anode is to be fear, which may lead to a damage of the detector.

3.3.2 Shifting zeropoint

Measurements

The next step was to fix the voltage difference between the three detector electrodes, but shift the overall potential with respect to detector chamber grounding, e.g., $U_{\mathrm{MCP_f}} = -778\,\mathrm{V} \rightarrow -578\,\mathrm{V}$, $U_{\mathrm{MCP_b}} = 1000\,\mathrm{V} \rightarrow 1200\,\mathrm{V}$ and $U_{\mathrm{P}} = 10\,222\,\mathrm{V} \rightarrow 10\,422\,\mathrm{V}$. With this method, the influence of the MCP-front voltage was investigated since the remaining performance of the detector should not change.

In previous experiments, for $U_{\mathrm{MCP_f}}$ below $-778\,\mathrm{V}$ an exceptionally high number of counts was found in a few camera pixels. This was attributed to unusual behavior of the double spots [17]. Thus, they are the focus of this section.

All of the used parameters are given in Table D.3.

Analysis and observations

First, a 2D-imaging plot filtered on doubles (sN = 2) was made for all runs (shown in Fig. E.1). For $U_{\mathrm{MCP_f}}$ below $-778\,\mathrm{V}$, the imaging pixels, approximately 255 px horizontal and 245 px vertical positions, show exceptionally high counts, almost double the ones in the beam center, i.e., the left plot of Fig. 3.8. The right plot shows non-such behavior.

An even more significant difference was visible at the impact-time difference distribution for doubles, as plotted in Fig. 3.9. The distributions show up to two extra peaks for voltages below $-778\,\mathrm{V}$, then the peaks disappear and are insignificant again.
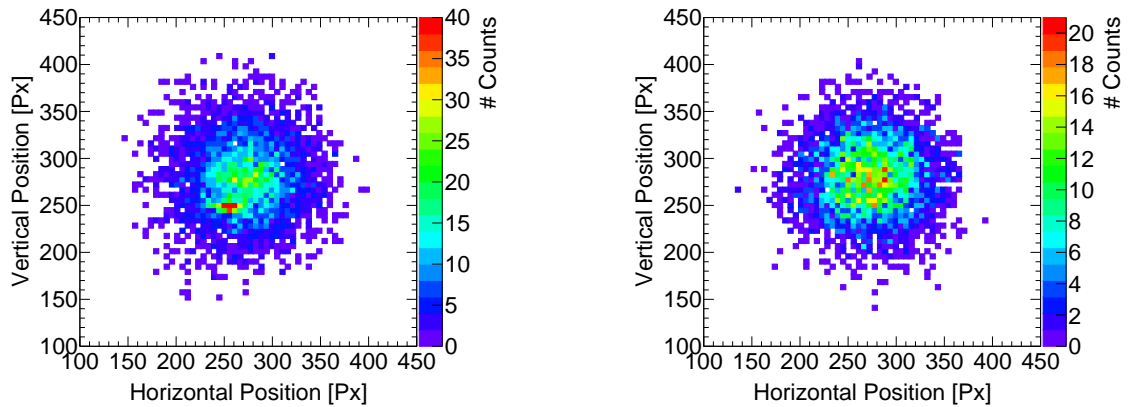

Figure 3.8: The left 2D-imaging plot shows the measurement with $U_{\mathrm{MCP_f}} = -1778\,\mathrm{V}$, the right one the measurement with $U_{\mathrm{MCP_f}} = -178\,\mathrm{V}$. Both plots are filtered on doubles.

Interpretation

The imaging plot shows an apparent anomaly for $U_{\mathrm{MCP_f}}$ below $-778\,\mathrm{V}$. These behavior could be explained by the scattering of positive ions from the MCP surface by the impinging fragments. This ions could be redirected through the electric field. That is, inside the channels the positively charged ions are accelerated in the opposite direction then the electrons. With negative MCP-front voltage, the electrical field outside of the MCP attracts the ions back to the MCP surface, where they can trigger a new event. The higher the MCP-front voltage with respect to ground, the more impact energy reaches the secondary ion and the more likely it is to detect the secondary impact. Also, the higher fields seem to lead to shorter delay of the secondary impact. And last, the inclination of the MCP channels lead to a similar transverse direction of the secondary ions with respect to their origin. This leads to a shifted secondary peak in the transverse position distribution. The double-time difference plot indicates two different ion types, for each peak one source.

For future measurements, a minimum $U_{\mathrm{MCP_f}}$ of $-778\,\mathrm{V}$ is recommended. Combining that result with that in sec. 3.3.1, a higher voltage is not recommended either, resulting in a lower bias voltage between the MCP and phosphor screen.
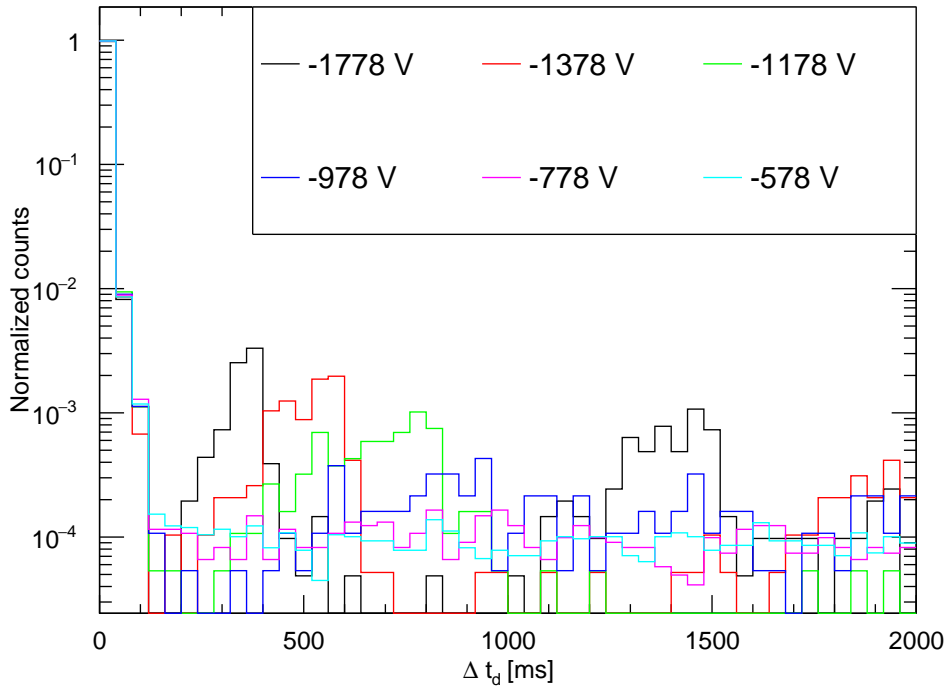

Figure 3.9: Shifting zeropoint. The graph shows the time difference between the registered doubles on an example of a few measurements. Due to lucidity, not all of the investigated bias voltages were not plotted.

3.3.3 Variation of MCP bias voltage

Measurements

After investigating the impact of $U_{\mathrm{MCP_f}}$ and U_{P}, the influence of the MCP bias voltage ($U_{\mathrm{MCP_{bias}}} = U_{\mathrm{MCP_b}} - U_{\mathrm{MCP_f}}$) remained to study. For this purpose, the previously discussed optimal MCP front voltage of $-778\,\mathrm{V}$ was kept constant. $U_{\mathrm{MCP_b}}$ and U_{P} were shifted by $50\,\mathrm{V}$ for each run. The different voltage settings are listed in Table D.4.

Due to higher MCP bias voltages, a stronger amplification is expected. Therefore, the SR445A amplifier was switched to one stage with an amplification factor of five.
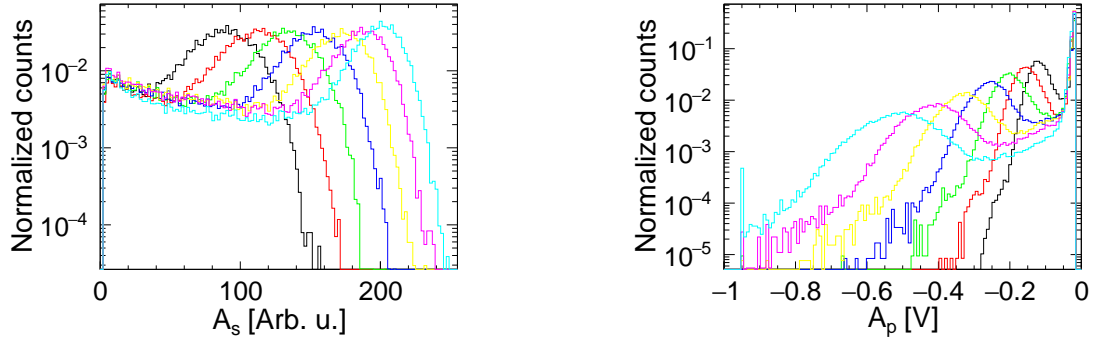

Figure 3.10: Spot and pulse height distributions for the investigated bias voltages. Black: $1778\,\mathrm{V}$, red: $1828\,\mathrm{V}$, green: $1878\,\mathrm{V}$, blue: $1928\,\mathrm{V}$, yellow: $1978\,\mathrm{V}$, pink: $2028\,\mathrm{V}$, turquoise: $2078\,\mathrm{V}$.

Analysis and observations

Fig. 3.10 shows the spot and pulse amplitude distributions. The peaks for both distributions shift to higher values, with a increasing $U_{\mathrm{MCP_{bias}}}$. Additionally, the pulse height distribution gets broader with increasing bias voltage. Otherwise, the peaks in the spot amplitude distributions get slightly narrower.

Furthermore, a COBRA analysis was conducted. The resulting fractions of invalid, valid and ambiguous events are presented in Tab. 3.4.

Interpretation

The outwards shift of the spot and pulse amplitudes is due to the more efficient electron cascade with a higher applied bias voltage on the MCP.

Just considering the spot and pulse height distributions, higher bias voltages are beneficial due to the clearer separation from the noise peaks.

However, the COBRA simulation shows the best result for $U_{\mathrm{MCP_{bias}}} = 1928\,\mathrm{V}$. The invalid and ambiguous events have their lowest probability at $1978\,\mathrm{V}$ and $1878\,\mathrm{V}$, respectively. This could be due to the width of the peaks. In principle, the broadening

$U_{\mathrm{MCP_{bias}}}$ [V]	Invalid [%]	Valid [%]	Ambiguous [%]
1778	8.6	59.7	31.7
1828	6.8	62.1	31.1
1878	6.2	66.3	27.5
1928	5.4	66.7	27.9
1978	5.2	66.2	28.6
2028	5.5	66.1	28.4
2078	5.7	65.6	28.7

Table 3.4: Results of the COBRA analysis for each run (see also Tab. 3.1).

of the pulse height distribution is good for COBRA. The parallel slight narrowing of the spot amplitude has the opposite effect. This combination could explain the maximum of valid events for $U_{\mathrm{MCP_{bias}}} = 1928\,\mathrm{V}$.

3.3.4 Dark count measurement

Measurements

Dark counts were visible and briefly described in previously presented plots. To get an overview of their influence, a night measurement was carried out, with only dark counts as the measurement goal. Moreover, the measurement should reveal possible inhomogenities of the detector. Hence, the beam was off. The measurement was performed with the standard settings of $U_{\mathrm{MCP_f}} = -778\,\mathrm{V}$, $U_{\mathrm{MCP_b}} = 1000\,\mathrm{V}$ and $U_{\mathrm{P}} = 11\,000\,\mathrm{V}$.

Analysis and observations

First, it was investigated whether the detector records evenly or has any irregularities. Latter should be visible from a 2D imaging plot,displaying the number of accumulated dark counts versus the transverse impact position (see Fig. 3.11). If examined more closely, one notices first the edges in the plot. Here the visible color spectrum differs from the one in the center. Inspecting a zoomed view of the edges, the visual color code implicates an inherent difference of events per bin. the second conspicuous feature is an apparent $\sim 20\,\mathrm{px}$ wide halo with higher counts of $\sim 200 - 250$ around the center. The other areas have stable count rates of $\sim 150 - 200$.

Next, the spot and pulse amplitude distributions were analyzed, see Fig. 3.12. For the pulse height distribution, the noise peak is visible. After, the spectra fall slowly until a break point ($A_{\mathrm{p}} = -0.6\,\mathrm{V}$), as the spot amplitude does ($A_{\mathrm{s}} = 120\,\mathrm{arb.u.}$). At this breaking point, both start to fall rapidly.
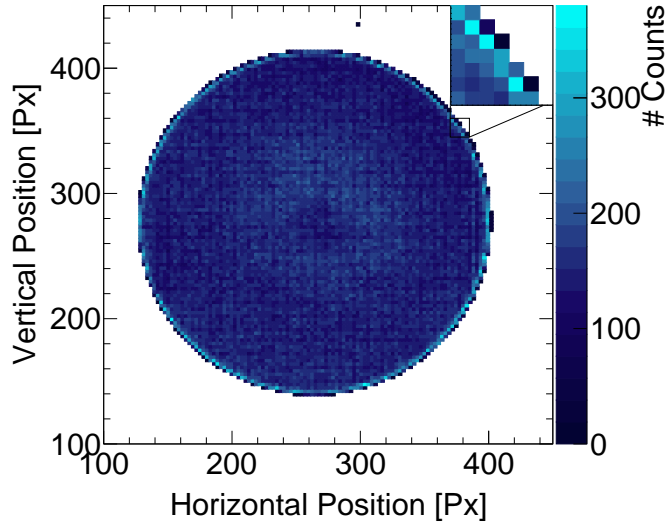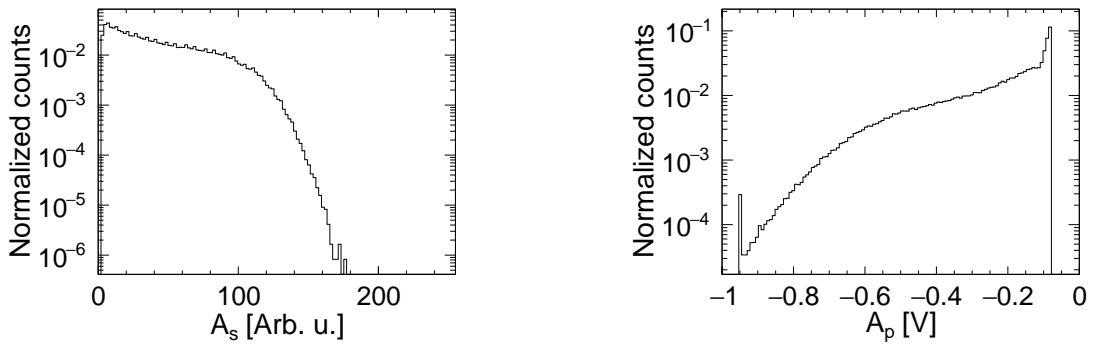
Figure 3.11: 2D-imaging.

Figure 3.12: Spot amplitude (left) and pulse height distributions of the dark count measurement.

Interpretation

In order to interpret the data, it is important to know what dark counts are to be expected. Up to this point, the theory assumes that the dark counts originate from cosmic rays and the internal radioactivity of the material of the MCP itself, resulting in two different sources.

If the dark counts result from cosmic rays, the detection must not start at the surface of the MCP front. It could be at each point within the MCP, direct at the phosphor screen or just the hit the camera. However, due to a low energy, it is assumed that the cosmic rays mainly triggers an avalanche within the MCP.

Due to small natural fraction of radioactive material in the glass material of the MCP, it is assumed the second dark count signal type starts an electron avalanche within the MCP.

However, due to the unknown trigger point, both sources should have broad amplitude spectra and could overlap. We neglect the thermal electrons as source of dark counts as these should be strongly suppressed at the $\sim 40\,\mathrm{K}$ MCP operation temperature.

The imaging picture shows a slight irregularity around the center of the positioning data. This could be from inhomogenities in the MCP material, which can be given by the manufacturing process, tension at the cryogenic temperatures, or traces of usage from the long term particle impacts, which indirectly lead to varying gain. Additionally, a few more suggestions could be made. First could the MCP have a slight irregular electric field, i.e. more particle with lower energies could be detected in this area. The same explanation could be for the phosphor screen. Due to the investigations in Sec. 3.3.1, this is unlikely since the difference in the field would need to be large. The third explanation could be the camera. The pixels in this area could be a little more sensitive than the rest and record particles with a lower energy. To fix this problem, further investigations are necessary.

The both amplitude distributions have a broad spectra, which declines to higher amplitudes. This is expected due to more needed energies for higher amplitudes. The noise spectra is also clear visible.

3.3.5 Saturation of the MCP

Measurements

Known from previous experiments, the recorded amplitudes of the NICE detector broke down at a count rate of a few kHz. For further investigations of the issue, this part of the measurements started with a high impact rate, which decreased during the injection cycle. The corresponding count rate is shown in Fig. 3.13. After 120 s, the beam was kicked out of the CSR.

To observe the behavior of the detector for different impact rates at the measurement start, each run was split in five schemes (explanation in Sec. C.2). For each scheme, the detector was switched on at a different storage time t_{start} of 1, 5, 10, 20 and 40 s. This timing setup was investigated with three different bias voltages, given in Table D.5.

These measurement setup should also explain the short and long term effects at the detector, after being exposed to a high impact rate.

Analysis and observations

In order to investigate the various schemes, the spot and pulse height amplitudes were plotted against the storage time for each scheme. After, the pulse height distribution for each time bin was analyzed and the mean value extracted with a
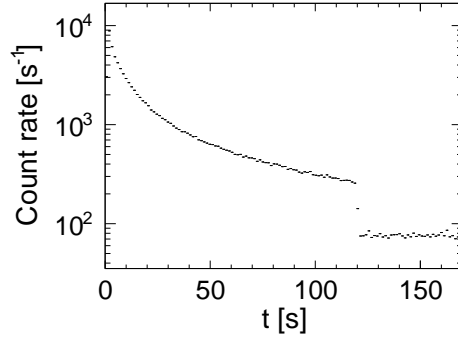
Figure 3.13: Count rate of run 50, scheme 0.

Gaussian fit for every scheme plot. Then these mean values were plotted over the storage time, shown in Fig. 3.14.

Scheme differences

Any amplitude of the respective scheme starts at the time the detector should have started to measure. For the first few seconds, the amplitudes decline a few seconds before reaching the curve of the previous scheme. After, the distributions are not to distinguish.

The amplitudes increase with a lower count rate.

Run differences

The analysis the different data sets, the pulse height mean values of scheme 0 were plotted over the time and further investigated with an exponential fit:

$$\exp(A^0 + x \cdot p) + A^{\text{offset}}. \tag{3.3}$$

Hereby, the offset value A^{offset} is the reached stable point. Furthermore, the time to reach 95 % of this position and $\tau = \frac{1}{p}$ were calculated. The three values are given in Tab. 3.5 for each bias voltages measurement.

The values show, that the time to reach this stable point is longer, the higher the bias voltage is. Additionally, the pulse height deflections increase.

$U_{\text{MCP}_{\text{bias}}}$ [V]	$t_{95\,\%}$ [s]	τ [s]	A^{offset} [mV]
1778	20.82 ± 0.19	-12.17 ± 0.10	-112.78 ± 0.06
1878	26.14 ± 0.14	-13.79 ± 0.07	-192.74 ± 0.08
1978	40.17 ± 0.22	-18.78 ± 0.10	-316.04 ± 0.17

Table 3.5: Offset and calculated values of τ and the time needed to reach 95 % of the offset height.

Interpretation

The non-differing amplitude evolutions between the various schemes at the same bias voltage give two possible interpretations of the saturation of the detector. TThe
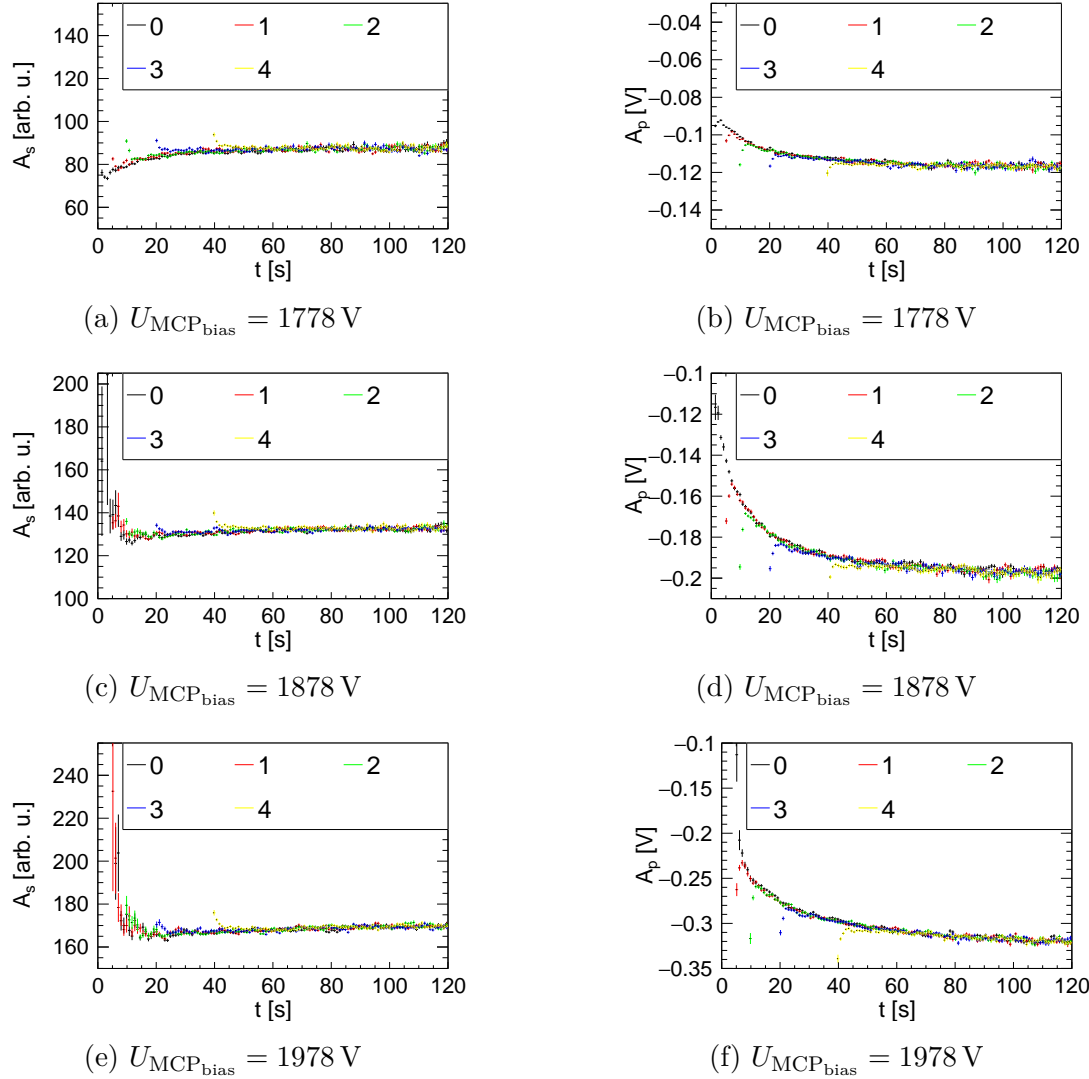
Figure 3.14: Mean values for the spot and pulse height amplitudes of each time bin of the time evolution plots. Left column: spot amplitude distribution, right column: pulse height distribution.

first interpretation is that the initial detector-off phase does not matter, i.e., that the detector is depleted also in the off phase. However, the initial higher amplitudes right after switching the detector on suggest a second, more likely interpretation: the detector saturates on a time scale of few seconds after switching the detector on - but the further behavior is independent of the history. This behavior will be further investigated at shorter time scales in Sec. 3.4.1.

The higher amplitudes for lower count rates has depletion reasons. For lower count rates, less electron avalanches get triggered. Thus, the MCP has more reserve to start avalanches more often and is parallel able to replenish the lost electrons. For high count rates, to much avalanches are triggered to replenish the electrons in

time. Thus, the amplify effect (gain) gets smaller and the amplitudes lower.

In summary, due to better spot and pulse distributions for lower count rates, it is recommendable to wait for lower count rates before starting the detector.

With a higher MCP bias voltage, the detector gets a better pulse height and spot amplitude for low count rates due to a stronger amplification of each hit. This is indicated through the different offsets for the various runs, given in Tab. 3.5. But, regarding the pulse height distributions, at high count rates the amplitudes start all near $\sim -0.1\,\mathrm{V}$. Presumably, the MCP is in saturation.

Another effect is the time to reach this stable offset and the given τ of the exponential function. Both significantly increase with a higher bias voltage. Thus, if operating the detector at higher count rates, a smaller bias voltage is recommendable to minimize the pulse height amplitudes. For the previous recommended bias voltage of $1778\,\mathrm{V}$ independently of the bias voltage, the count rate should not be higher than $\sim 2 \times 10^3\,\mathrm{s^{-1}}$ to change the mean amplitudes by less than $\sim 10\,\%$.

In summary, it is not recommendable to operate the detector at high count rates. If high count rates are necessary, a lower MCP bias voltage would be preferable to prevent the saturation of the detector. However, for count rates below $\sim 2 \times 10^3\,\mathrm{s^{-1}}$ a higher bias voltage improves the pulse height and spot amplitudes.

3.4 Detector switching

The measurements before this thesis were mostly performed with a maximum count rate of $\sim 2\,\mathrm{kHz}$, else the detector was in saturation. As shown in Sec. 3.3.5, higher impact rates lead to a significant collapse of the pulse height amplitudes. However, for planned future experiments, the detector needs to be capable operating at significantly higher impact rates without risking a collapse of the pulse height amplitudes or damaging the detection system. On the other hand, in many applications it is not necessary to continuously detect all impacted fragments, but it is sufficient to keep the counting and imaging capability at a reduced detector operation duty cycle. Therefore, a new method to operate the detector was tested and discussed in this part of the thesis.

Here, instead of operating the detector continuously, the MCP front voltage is technically switched on and off between the nominal value and ground potential rapidly with an implemented pulse generator. Thus, the electron avalanches are suppressed during the off phase of the detector. In this time, the MCP channel walls have time to replenish the lost electrons. Coincidentally, the on period is not long enough to reach a saturation point. As a result, the recorded count rate just applies for the detector on phase. In order to obtain the expected count rate for a continuously operating detector, it should be possible to recalculate it (see Sec. 3.4.3).

Before implementing, the mode has to be tested first and the optimum settings had to be found. New parameters such like the switching frequency and the duty cycle were added to the already known ones. But first of all, the recovery time after the depletion phase has to be known. After the impact of the switching parameters were investigated, such as the switching frequency, duty cycle and off voltage. Last, an equation was implemented to calculate the impact rate, equivalent to the count rate obtained in the continuous mode discussed above.

3.4.1 Depletion and recovery time

Measurements

Before beginning with fast switching, the recovery and depletion time at full saturation have to be understood in detail. Thus, the following scheme was repeated in each injection cycle: The detector is switched off at the time of injection the ions, and is switched on only at $220\,\mathrm{ms}$. At a defined time t_{off} the detector is switched off again for a time range of $40 - 700\,\mathrm{ms}$ (value fixed within one measurement set). At $t = 1200\,\mathrm{ms}$ the detector is than switched on again to observe the recovery status. The amount of detector depletion and recovery is evaluated from the temporal changes in the pulse height distribution.

Two measurement series for different count rates were carried out. The first measurement series start with an initial count rate of $\sim 10^4\,\mathrm{s}^{-1}$. The parameters for the various runs are given in Tab. D.6. The second measurement series was carried

out with a count rate of $\sim 6 \times 10^3 \, \text{s}^{-1}$. The different times and settings are given in Tab. D.7.

Analysis and observations

Fig. 3.15 shows the pulse height time evolution plot for, e.g., time gaps of (left) 700 ms and (right) 40 ms for the high count rate measurements of $\sim 10^4 \, \text{s}^{-1}$. For both plots, pulse amplitude changes for few 100 ms before reaching a stable, saturated value. Thereby, pulse amplitudes drops (here: less negative values). After the off phase, A_s recovers to higher amplitudes again. The recovery level depends on the duration of the off-phase. During the second on-period the pulse heights start to degenerate again.

To investigate the time frame of the degenerating amplitudes, the two runs with the shortest t_off time for the first degeneration time and the ones with the largest t_off time were fitted with Eq.:

$$-\exp\left(A^0 + xt\right) + A^\text{offset}. \tag{3.4}$$

From this equation, two values were calculated. The first value was $\tau = \frac{1}{t}$, the second the time which the curve need, to reach 95 % of the offset value. These values and the offset value are given in Tab. 3.6.

gap position	gap [ms]	τ [ms]	$t_{95\,\%}$ [ms]	A^offset [mV]
before	50	80.19 ± 0.90	208.33 ± 5.55	-78.96 ± 0.10
after	700	191.20 ± 5.12	451.20 ± 55.76	-83.98 ± 0.44
before	50	105.37 ± 1.90	202.12 ± 8.77	-97.08 ± 0.10
after	700	228.31 ± 13.03	407.96 ± 114.49	-98.54 ± 0.67

Table 3.6: The first two rows refer to the measurement series with a count rate of $\sim 10^4 \, \text{s}^{-1}$, the last two ones to the measurements with a count rate of $\sim 6 \times 10^3 \, \text{s}^{-1}$. τ is calculated from the received fitting parameter, $t_{95\,\%}$ is the time to reach 95 % of the height of the offset, and the received offset A^offset of the fitting parameter.

In order to investigate the recovery time of the detector, the pulse amplitude distribution of the first $\sim 29 \, \mu\text{s}$ (the first five bins) at the start and after the gap was fitted with a Gaussian distribution. The obtained mean values were subtracted from each other and plotted, see Fig. 3.16. After, the two curves were fitted by an exponential function[1]. With these, the replenish time to reach 10 % of the initial value were recalculated. For the initial value, the measurement with the shortest gap was taken. The received parameters and results are presented in Tab. 3.7.

In order to compare the received τ with the theoretically one calculated in Sec. 2.2, it is calculated at which time scale one single channel is triggered. Therefore,

---

[1]Function given by [18]: $\exp\left(p0 + p1 \cdot x\right)$
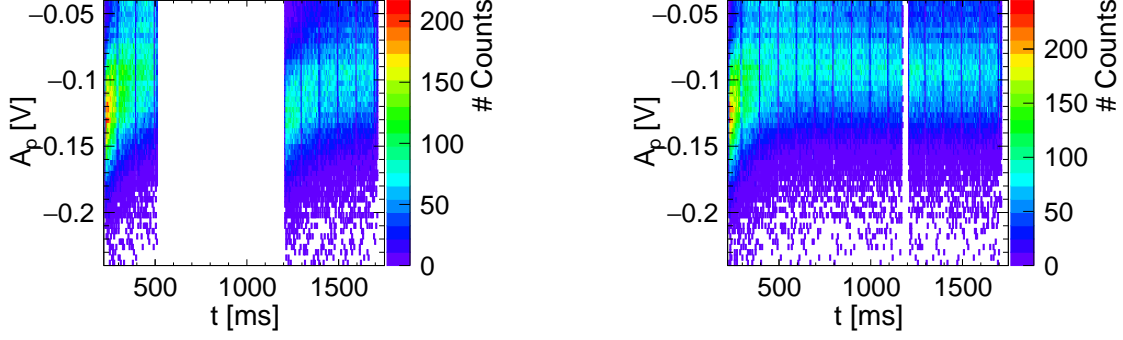
Figure 3.15: Time evolution plot with a gap of (left) 700 ms and (right) 40 ms for high count rate measurements of $\sim 10^4\,\mathrm{s}^{-1}$

the number of the channel of which the beam triggers is calculated. In this case, a beam radius over $\sim 100\,\mathrm{px}$ is assumed (taken from Fig. 3.2). With a factor of $\sim 0.4\,\mathrm{mm\,px^{-1}}$ an area of $A = \pi \cdot (20\,\mathrm{mm})^2 \approx 1250\,\mathrm{mm}^2$ is triggered. Each channel has an diameter of $25\,\mu\mathrm{m}$ and the open area ratio is assumed to be $\sim 60\,\%$. Thus, the channel number is:

$$N = \frac{0.6 \cdot \pi\,(20\,\mathrm{mm})^2}{\pi\,(12.5 \times 10^{-3}\,\mathrm{mm})^2} \approx 1.5 \times 10^6. \tag{3.5}$$

The time between each trigger for one channel can now be calculated from the different count rates:

$$t_{10} = \frac{1.5 \times 10^6}{10 \times 10^3\,\mathrm{s}^{-1}} = 150\,\mathrm{s} \qquad \text{and} \tag{3.6}$$

$$t_6 = \frac{1.5 \times 10^6}{6 \times 10^3\,\mathrm{s}^{-1}} = 250\,\mathrm{s}. \tag{3.7}$$

Count rate	τ [ms]	initial value	$t_{10\,\%}$ [ms]
10×10^3	187.27 ± 4.56	29.90 ± 0.29	461.56 ± 11.93
6×10^3	192.79 ± 1.71	20.96 ± 0.41	485.28 ± 5.90

Table 3.7: Calculated τ and time to reach $10\,\%$ of initial pulse height amplitude of the fit functions in 3.16.

Interpretation

The measurements series shows that the MCP depletion occurs on a time scale of $t_{95\,\%} \approx 200\,\mathrm{ms}$, and that then an equilibrium is reached where the amplitudes do not degrade further. The second time it needs with $\sim 425\,\mathrm{ms}$ more than double that time. This time difference could be due to the decaying count rate across
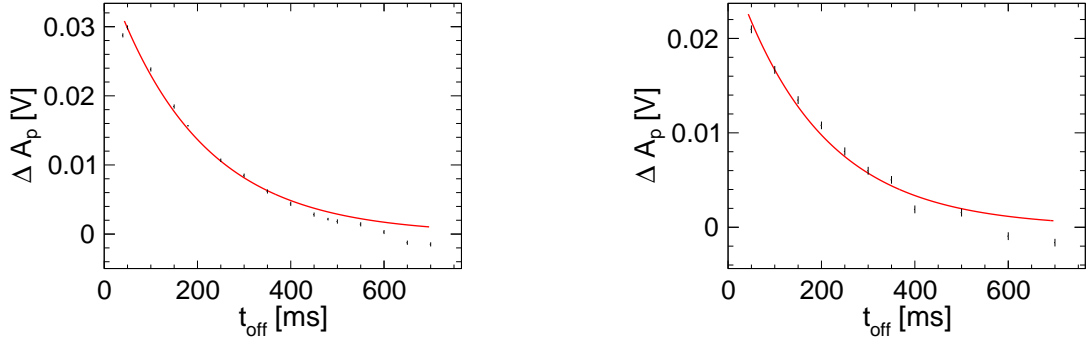
Figure 3.16: Difference between the mean value of the first five bins before the gap and after the gap. Left: measurement series with a count rate of $\sim 10^4\,\mathrm{s}^{-1}$, right with a count rate of $\sim 6 \times 10^3\,\mathrm{s}^{-1}$

the duration of the measurement, which could also explain the high count rates at the start. Hence, more electrons are dissolved due to the higher rate of impinging fragments, which is not the case for later times. Another option would be, that the exponential fit function does not represent the data properly enough and more data would be needed, which the high errors indicate and also the shift of the pulse height offset for the first measurement. On the other hand, this dependence for the recovery time of the count rate is also indicated trough the τ values before the gap. Here, both values have a significant discrepancy of $\sim 25\,\mathrm{ms}$. The measurement with the higher count rate reaches faster the equilibrium state than the measurement with the lower count rate.

As discussed before in Sec. 3.3.5, higher count rates lead to a decreasing pulse height amplitudes. Regarding the different offset values of the two different count rate measurements, this is here the case too.

To fully recover the MCP charge, the detector has to be off for nearly 500 ms. However, it should not be an impediment for fast switching, since the recovery for small time gaps is almost negligible.

Compared to the calculated replenish time of 25.48 ms in Eq. 2.4 the received values of $\tau = (187.27 \pm 4.56)\,\mathrm{ms}$ and $\tau = (192.79 \pm 4.56)\,\mathrm{ms}$ is almost eight times higher. This should be not the case, since the time to trigger one channel is for both count rates at in order of 100 s. Thus, each channel should already has replenished its electrons. Since this is not the case, one has to assume, that the channels are not independent from each other and also influence the channels in the near area.

Also the beam intensity has no big influence at the recovery time. The calculated times at 10 % of the initial values are within a 2σ range.

3.4.2 Measurement times

From here on, all measurements were taken with an injection cycle duration of 10 s, with the ion stored for 7 s. The detector is switched off for the first 1 s, then

the periodic switching starts. Unless otherwise stated, the voltages are fixed at $U_{\mathrm{MCP_f}} = -778\,\mathrm{V}$, $U_{\mathrm{MCP_b}} = 1000\,\mathrm{V}$, $U_{\mathrm{P}} = 10\,700\,\mathrm{V}$, and a switching off voltage of $U_{\mathrm{MCP_f}}^{\mathrm{off}} = 0\,\mathrm{V}$. The initial count rate at $t = 1\,\mathrm{s}$ is at $20 \times 10^3\,\mathrm{s}^{-1}$. Thereby, the influence of the switching frequency, the duty cycle and the switching voltages were investigated.

In Tab. D.8 are the different measurement settings given for different switching frequencies. Tab. D.9 contains the different duty cycle measurements. The settings for the different off voltages can be found in Tab. D.10, where a power supply has been connected in order to adjust the different off voltages.

Analysis and observations

In order to investigate the behavior of each switching cycle, some parameters have to be understood first:

Reference time t_{ref}

In the new mode, the detector switches on and off in a short amount of time for each switching cycle. This *reference time t_{ref}* is determined through the adjusted frequency f and defined by each switching cycle:

$$t_{\mathrm{ref}} = \frac{1}{f}. \tag{3.8}$$

Detector on time $t_{\mathrm{ref}}^{\mathrm{on}}$

Due to the duty cycle, the above introduced time includes the on and off times of each switching cycle in %. In order to just analyze the data of the on measurement, it is useful to know the actual recording time in each cycle. This time is determined by the duty cycle (see Sec. C.1) and can be calculated with an extension of equation 3.8:

$$t_{\mathrm{ref}}^{\mathrm{on}} = \frac{1}{\mathrm{f}} \times \frac{\mathrm{d}}{100}. \tag{3.9}$$

The different runs were all analyzed through a time evolution plot of the pulse height amplitudes over a reference time of $t_{\mathrm{ref}} = 2\,\mathrm{ms}$. Even if this time not cover all of the detector on times $t_{\mathrm{ref}}^{\mathrm{on}}$, it will be enough to investigate the temporal evolutions of each plot. All measurements were analyzed as in the following scheme, demonstrated at run 158, with a switching frequency of $f = 50\,\mathrm{Hz}$ and a duty cycle of $d = 20\,\%$.

The pulse height amplitude was drawn up to reference time range of $0-2\,\mathrm{ms}$, given in Fig. 3.17 (left). Inspecting the time evolution plot, the pulse height peak increase to a stable point. Thus, the vertical slices (a pulse-height distribution in given time bin) was fitted with a Gaussian distribution, as explained in Sec. 3.2.The temporal

evolution of the so obtained central values was fitted further by an exponential function with an offset[1], shown in Fig. 3.17 (right).

With the received parameter the time to reach 95 % of the stable point were calculated. In addition, Tab. 3.8, 3.9, 3.10 gave the offset of each section.
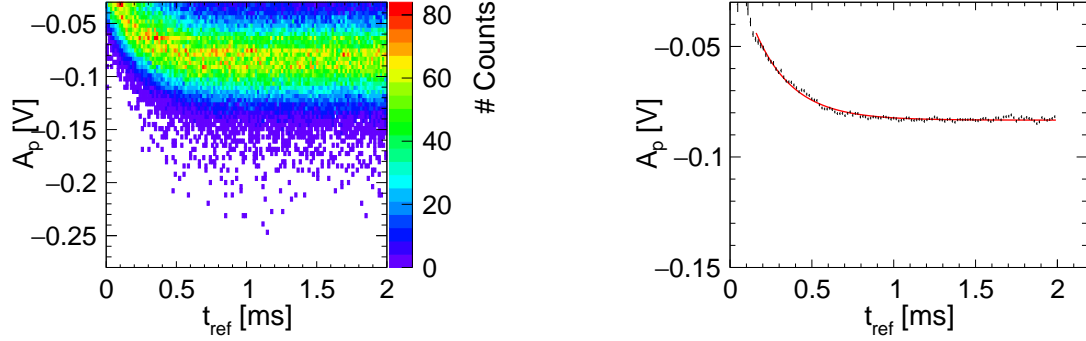

Figure 3.17: Reference time evolution (a) zoomed in on 2 ms and the associated mean value plot with an exponential fit.

#	f [Hz]	τ [μs]	$t_{95\%}$ [μs]	A^{offset} [mV]
1	10	-247.68 ± 11.18	710.36 ± 35.99	-86.47 ± 0.20
2	50	-230.81 ± 3.56	678.06 ± 11.45	-83.33 ± 0.08
3	100	-276.75 ± 3.87	743.38 ± 11.51	-78.35 ± 0.06
4	500	-172.08 ± 7.19	476.61 ± 31.30	-72.54 ± 0.83

Table 3.8: Results for the frequency measurement series with a applied duty cycle of 20 %.

#	d [%]	τ [μs]	$t_{95\%}$ [μs]	A^{offset} [mV]
6	1	-33.40 ± 2.71	243.11 ± 13.41	-66.07 ± 0.77
7	5	-201.26 ± 2.10	586.29 ± 6.45	-90.22 ± 0.11
8	20	-218.51 ± 3.15	647.05 ± 10.16	-79.96 ± 0.08

Table 3.9: Results for the duty cycle measurement series with a applied frequency of 50 Hz.

Interpretation

The interpretation of the analysis will be in two steps, first the start of each switching cycle is discussed, after the pulse height deflection.

---

[1] $\exp(A^0 + x\tau) + A^{\text{offset}}$

#	U^{off} [V] [Hz]	τ [μs]	$t_{95\%}$ [μs]	A^{offset} [mV]
10	100	-258.19 ± 4.42	764.30 ± 14.26	-80.79 ± 0.10
11	200	-264.69 ± 4.14	789.12 ± 13.40	-84.64 ± 0.10
12	300	-279.68 ± 3.90	823.67 ± 12.31	-90.90 ± 0.10
13	400	-280.45 ± 3.85	843.04 ± 12.39	-91.74 ± 0.10
14	500	-270.80 ± 3.63	840.04 ± 12.15	-91.64 ± 0.10
15	600	-276.97 ± 3.73	859.39 ± 12.48	-91.68 ± 0.10
16	700	-271.15 ± 3.84	864.06 ± 13.27	-91.48 ± 0.11

Table 3.10: Results for the switching voltage measurement series with a applied frequency of 50 Hz and duty cycle of 20 %.

Stabilization Phase

At the start of each switching cycle, i.e., after the detector is switched on by setting the nominal bias voltage value, the detector needs a short time to measure with full amplitude. Thus, the detector should be long enough on to reach a stabilization phase. This period can be calculated with Eq. 3.9. The measurements with the lowest duty cycle of 1 % and highest frequency of 500 Hz never reached this stable point, which is already visible in the reference time evolution plots (see E.2). Hence, these two measurements will be not considered in the following.

The calculated times to reach a full amplitude of 95 % could give a hint on the length of the stabilization phase. Here, the range varies between $(586.29 \pm 6.45) - (864.06 \pm 13.27)\,\mu$s. Thus, the measurement time should not be less than 1 ms to guarantee to measure at least a short period of the stable pulse height phase. These times can be calculated with Eq. 3.9 for each parameter setting.

In the following are the τ values compared to each other, due to less fluctuations.

Comparing the $f = 50\,$Hz (No. 2) to the 20 % measurement of the duty cycle measurement series (Tab. 3.9, No. 8) an identical measurement setup can have some fluctuations. Besides the fluctuations in each measurement, this could also be a fitting problem. However, the two measurements are still in a 3σ-range.

Consider just the switching frequency measurements (Tab. 3.8), the frequency seem to have no influence of the stabilization phase. However, to confirm this more measurements are needed.

The measurement series varying the duty cycle is rather short, see Tab. 3.8. Just the run with $d = 20\,\%$ reach a $t^{\mathrm{on}}_{\mathrm{ref}} > 2\,$ms. Thus, it is not possible to make a statement, if the duty cycle influences the time to stabilize or not. Though one can well assume that for large duty cycle values (i.e, short off-phases) the detector cannot recover fully in the off-phase and thus also the initial stabilization after switching the detector on can be affected.

Due to the huge variation between two identical cycles, it is difficult to make a statement for the last measurement series, whereby the switch-off voltages were changed. However, in Tab. 3.10 a direction is recognizable. With each higher off-voltage, the time to stabilize the peak slightly increases. Thus, the detector needs

longer to switch on. One reason for this growth, could also be the increasing pulse height amplitudes, which will be discussed next.

Pulse height deflection

Besides the stabilization time, the recorded pulse height deflections varied also. This deflection can be determined by the received offset parameter of the exponential fit.

Contemplating the switching frequencies (Tab. 3.8), lower switching cycles ensure higher pulse height amplitudes. This is due to the off time, which is to the detector off time in each switching cycle of 80 ms for the 10 Hz, 16 ms for the 50 Hz, and 8 ms for the 100 Hz measurements. In Sec. 3.4.1 was already discussed, that at an off time below 50 ms was no recovery effect visible. However, it results that below these value still some effects are to observe.

The measurement series investigating the duty cycle again contains too few measurements to make a conclusive statement.

The last six runs, on the other hand, give a clear picture again, see Tab. 3.10. Up to off voltages of 400 V, the pulse height deflections increase from (-80.79 ± 0.10) mV to (-91.74 ± 0.10) mV. After, the offset stagnates. That is, that the off voltages over this value ensure a higher replenishment rate of the electrons in the MCP channels. Following these thought, for future experiments it will be useful to set a higher off voltage of at least 400 V.

3.4.3 Count rate and the influence of switching

Switching the duty cycle in a fast manner was implemented to measure with much higher impact rates without saturating or damaging the detector. To use it for future experiments, it has to be know how the count rate scales with the new settings. For this purpose, an assumption was made based on the expected count rate in the standard mode.

Recalculated count rate

Due to the new recording method, the detector only measures a part of the impinging fragments. However, it is essential to know their total number. Thus, the count rate must be corrected and recalculated with the following formula:

$$\text{expected impact rate} = \text{count rate} \times \frac{100}{\text{d}}. \tag{3.10}$$

I.e., the count rate scales with a factor given by the duty cycle. Fig. 3.18 shows such a recalculated count rate (b) and compared it with a previous measurement without fast switching (a) performed at the same conditions (also the same ion beam intensity and thus the same impact rate). Hereby, the count rate of the fast switching section was recalculated from 2 kHz to 10 kHz, which is comparable to the right plot.

Pulse height amplitudes

Under the count rate plots in Fig. 3.18 are the associated pulse height amplitudes (c), (d). Both plots show the in Sec. 3.2 described shape with a noise peak at the right side of the spectra up until $\sim 0.03\,\text{V}$. Nevertheless, the pulse height for the fast switching measurement has a much clearer separation from the noise peak and a more pronounced shape than the pulse height distribution measured in the standard mode. Thus, the fast switching not only prevents the detector for being damaged, but also improves the measured data.

It follows that the expecting count rate defines the duty cycle. However, the count rate should not exceed $2 \times 10^3\,\text{s}^{-1}$, since damage is also to be feared above this value.
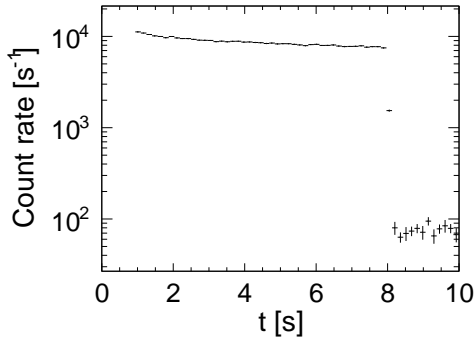
(a) Count rate plot for the normal mode
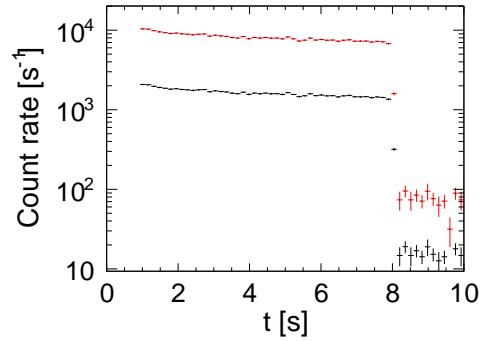
(b) Count rate plot for the switching mode
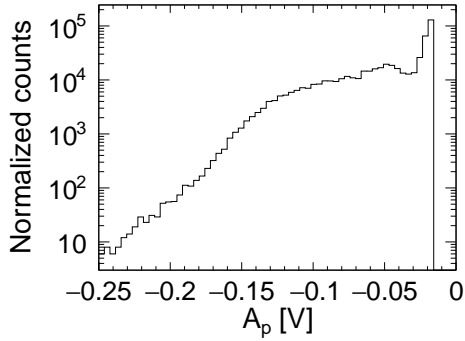
(c) Pulse height plot for the normal mode
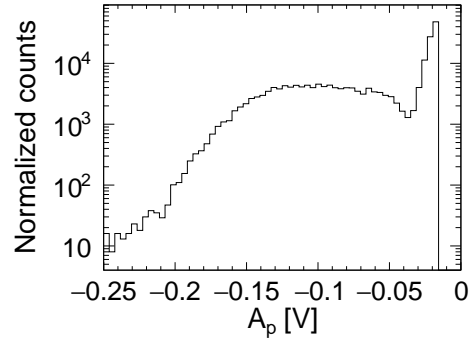
(d) Pulse height plot for the switching mode

Figure 3.18: Comparison of count rate and pulse height plots with the same beam intensity for the standard and switching mode, with a frequency of $f = 10\,\text{Hz}$ and a duty cycle of $20\,\%$.

Varying the duty cycle

To vary the above given calculation, the count rates of the duty cycle measurement series was plotted and recalculated, given in Fig. 3.19. A fourth plot was made with a different frequency, to ensure no influence of this parameter.

All runs have a similar recalculated count rate of $20 \times 10^3\,\mathrm{s}^{-1}$, whereas the measured count rate changes with each duty cycle variation. Thus, for these measurements the formula is correct.

As expected, the frequency has no influence and has not to be considered for recalculation. The plots (c) and (f) differ only on some individual measurement points.

(a) duty cycle 1 %

(b) duty cycle 5 %

(c) duty cycle 20 %

(d) duty cycle 20 %, $f = 10\,\mathrm{Hz}$
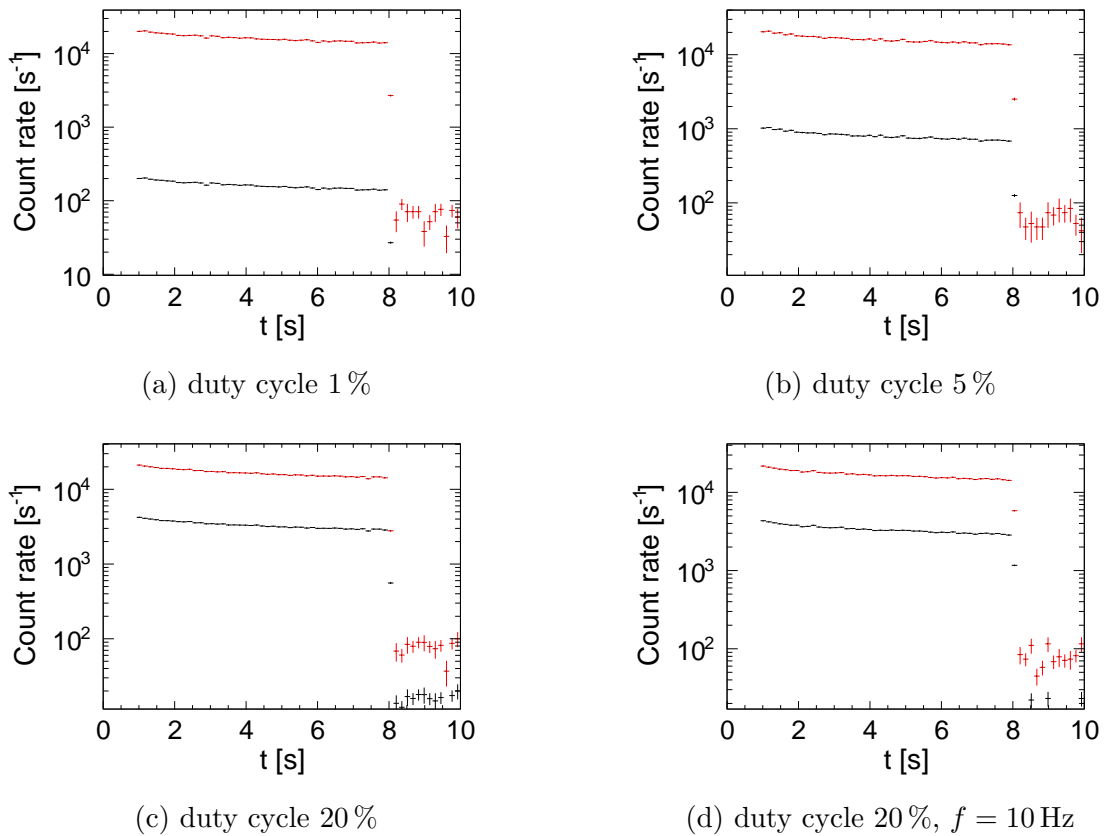
Figure 3.19: Count rate plots for different duty cycle.

3.4.4 CF$^+$

Until this point, all measures data were taken of residual-gas collision with a $O_2{}^+$ beam. To verify the function of the fast switching mode, a re-measurement was taken in February 2022 with CF$^+$, also as residual-gas collision. The detector settings were set at $U_{\mathrm{MCP_f}} = -778\,\mathrm{V}$, $U_{\mathrm{MCP_b}} = 1000\,\mathrm{V}$ and $11\,\mathrm{kV}$. The front voltage were switched with respect to the ground. The measurement were taken over a time of $23.1\,\mathrm{s}$, with an off time of $4.2\,\mathrm{s}$ and an on time of $18.9\,\mathrm{s}$.

The measured count rate is $8 \times 10^2\,\mathrm{s}^{-1}$, thus, the recalculated count rate with Eq. 3.10 is $\sim 2 \times 10^4\,\mathrm{s}^{-1}$. This is also confirmed by Fig. 3.20 (a).

Fig. 3.20 (b) shows the pulse height distribution. A broad peak with a clear to distinguish noise peak is visible. Thus, the switching mode with the right parameter allows to record pulse height amplitudes with much higher count rates without fearing of saturation effects or a collapse of the pulse height.

(a) Count rate

(b) Pulse height distribution
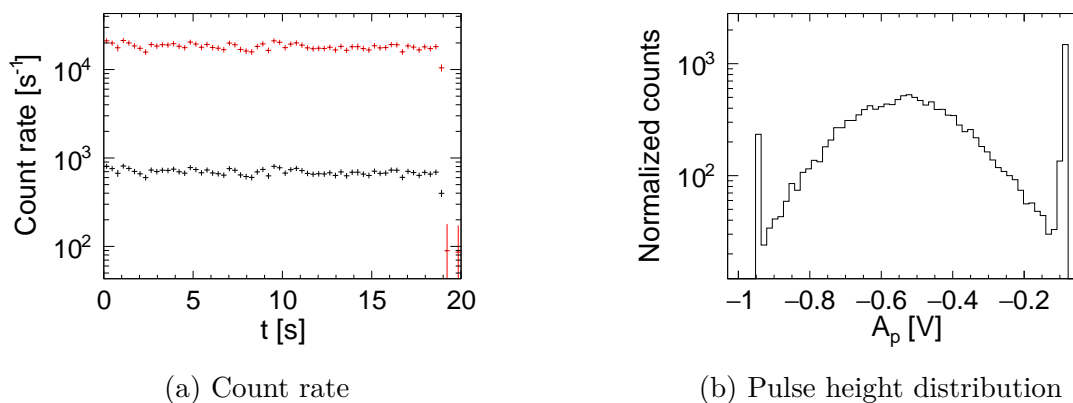
Figure 3.20: The count rate plot, with the measured rate (black) and the recalculated rate (red) and the received pulse height distribution for a fast switching measurement with CF$^+$.

4 Conclusion

Over a course of this bachelor project, the NICE detector was systematically investigated and characterized. Thus, NICE was operated in a one-week CSR beamtime, detecting neutral products from $O_2{}^+$ collisions with residual-gas with different beam intensities and detector settings. Thereby, the optimal detector settings should be elicit. Furthermore, a new switching mode to operate the detector was implemented and tested in order to increase the $2 \times 10^3\,\mathrm{s}^{-1}$ count rate maximum.

The first part of this thesis discusses the assessment of the optimal detector settings. It could be verified that higher bias voltages between the MCP front and back as well as between the MCP back and phosphor screen lead to higher spot and pulse height amplitudes. However, due to the fear of damaging the detector setup, the bias voltage between the MCP front and back are restricted to $\sim 1800\,\mathrm{V}$, even if a bias voltage of $\sim 1900\,\mathrm{V}$ would reveal better COBRA results. In fact,, during the measurement week, an amplifier was already damaged due to a bias voltages of $1878\,\mathrm{V}$. Furthermore, measurements at high count rates show an opposite picture. Here smaller bias voltages show less saturation effects for the pulse height amplitudes. The second found restriction is on the MCP-front voltage with $\sim -800\,\mathrm{V}$. At more negative voltages, the detector records non-negligible amount of fake-double events from positive-ion acceleration in the MCP channels. Considering all aspects, the settings for future experiments should be close to $U_{\mathrm{MCP_f}} = -778\,\mathrm{V}$, $U_{\mathrm{MCP_b}} = 1000\,\mathrm{V}$ and $U_\mathrm{P} = 11\,\mathrm{kV}$ for a maximum count rate of $\sim 2 \times 10^3\,\mathrm{s}^{-1}$. It was also found that lowering the MCP bias voltage by $\sim 800\,\mathrm{V}$ effectively switches the detector off so that it does not get depleted. Correspondingly, even very high impact rates during the detector-off phase do not affect the detector behavior after switching it on again and operating at low impact rates.

Another aspect was to investigate irregularities at the detectors surface by investigating spacial distribution of the dark counts over a long time frame. Here in the 2D-imaging view, small changes can be seen in form of a halo around the detector center in the imaging pictures. Where these originate could not be determined. A possible explanation could be the extensive usage of the detector in the last few years, since this area should be the most stressed.

n the second part of the thesis the detector behavior was investigated while switching it periodically on and off - this scheme was chosen in order to lower the saturation effects (MCP electron depletion) and thus also pulse height distribution distortions at impact rates $> 2 \times 10^3\,\mathrm{s}^{-1}$.

It was found that after switching the detector on at high impact rates the pulse heights decay on a time scale of $\sim 200\,\mathrm{ms}$ to reach a saturated level. The decay is faster for higher impact rates. This decreasing is due to the depleting electrons in

the MCP walls until an equilibrium is reached, between the dissolving electrons and replenishing electrons.

On the other hand, the measured recovery time (duration of the off-phase) displays an exponential behavior with $\tau \approx 190\,\mathrm{ms}$. In our setup this time is much shorter than typical time for hitting the same MCP channel repeatedly. Therefore, it is assumed that the simple capacitor model for the MCP-recovery cannot be valid. This is also supported by the fact that the recovery time from that model is only $\sim 25\,\mathrm{ms}$, i.e., $\sim 8\times$ shorter than the experimentally derived times. No recovery time is to observe for a detector of period of $50\,\mathrm{ms}$. Thus, future measurements should be longer than $500\,\mathrm{ms}$. Furthermore, $50\,\mathrm{ms}$ should be the upper time limit for the off-times in the detector switching mode, if clear pulse height amplitudes are requested.

It is realized that the detector depletion time is by a factor two smaller than the recovery time. Therefore to keep the depletion low in a switched detector operation the off-phase should be significantly longer than the on-phase, and the on-phase must stay significantly shorter than the saturation time of $\tau \approx 100\,\mathrm{ms}$. These time restrictions can be calculated with Eq. 3.9. In combination with Eq. 3.10 both equations determine the frequency f and duty cycle d for each setup.

A lower limit of $\sim 1\,\mathrm{ms}$ for the on-period duration was also determined . This is because after switching the detector on the pulse heights reach the nominal values only after this minimal time. For better pulse height amplitudes, it is also recommendable to set the off-state MCP bias voltage higher than $\sim 1200\,\mathrm{V}$ in the switching mode. Thus, the electrons replenish faster in each off-period.

The fast-switching mode was also successfully demonstrated in a CF^+ beam time for count rates up to $\sim 2 \times 10^4\,\mathrm{s}^{-1}$ with no significant pulse height distortion. Thus, the above discussed findings are not just restricted to the $\mathrm{O_2}^+$ measurements. Afterwards even impact rates of $\sim 10^5\,\mathrm{s}^{-1}$ were used in an $\mathrm{H_2D}^+$ beam time - there the pulse heights were distorted already, but the counting was still reliable and even 2D-imaging data were available.

All in one, the switching mode for the detector is possible and an option to measure higher impact rates without fearing to damaging the detector and at the same time still get good pulse height distributions.

5 Outlook

Due to time restrictions, not all data collected for this thesis were analyzed yet and a few data just partly, e.g., the analysis in Sec. 3 were just analyzed regarding the pulse height amplitudes. However, the spot amplitudes also contains interesting and important information, especially for the COBRA principle. Other not yet analyzed data are measurements considering, for example, the influence of the detector temperature or extreme duty cycles.

One of the practical results of the thesis is the observation that lower MCP bias voltage in the off-state would improve the re-charging . Given the other constrains (e.g., the maximal MCP-front voltage to avoid fake-doubles) we will need to implement an additional power supply for the off-voltage of MCP-front electrode - an easy thing to do. Similarly, implementing a more robust amplifier would allow for using higher MCP bias voltages, which is advantageous for the COBRA principle.

Furthermore, an investigation of the electric circuit could be aspired.

In order to obtain a reliable 3D-imaging, stable pulse height amplitudes combined with imaging data are important. However, due to the switching-on phase of $\sim$ 0.5 ms and the camera readout time of $\sim$ 1 ms the time restrictions could lead to issues regarding imaging for very short on periods. Thus, the Data aquisition system (DAQ) should be modified, so that the camera can trigger only after the 0.5 ms.

Besides these suggestions, Jäger [5] already started a project on implementing a SiPM array for optical readout of the NICE detector, which would provide better timing information compared to the anode signal, especially for fragments impacting close in time. Once finished, this additional readout will provide more freedom for the COBRA analysis and thus also less restrictions on the amplitude distributions discussed in this thesis.

The one efficiency of the NICE detector is the fact that it cannot provide information on the mass of the impacting fragments. To improve on this, NICE will be complemented by a micro-calorimeter based Molecular Camera (MOCCA) detector which can provide not only the impact positions but also kinetic energies (and thus also masses) of the individual molecular fragments. The MOCCA detector is planned to be implemented directly behind the NICE, which has also influences on the detector. [19] [20]

Part I

Appendix

A Acronyms

CSR Cryognic Storage Ring

COBRA Correlation of Spot Brightness and Pulse Amplitude

NICE Neutral Imaging in Cold Environment

DR Dissociative Recombination

COMPACT Cold Movable Particle Counter

RF Radio Frequency

MPIK Max Planck Institut für Kernphysik

MCP Microchannel Plate

GIDS German Imaging Detector Solutions

CMOS Complementary Metal-Oxide Semiconductor

MOCCA Molecular Camera

SiPM Silicon Photomultiplier

DAQ Data aquisition system

B Lists

B.1 List of Figures

B.2 List of Tables

Part II

Appendix

C Measurements

C.1 Duty cycle d

The duty cycle indicates the ratio between the recording and relaxing time during the total operated time of a device. [21]

Fig. C.1 visuals a $20\,\%$ duty cycle. For each frequency period, the voltage is off for $80\,\%$ of the time.

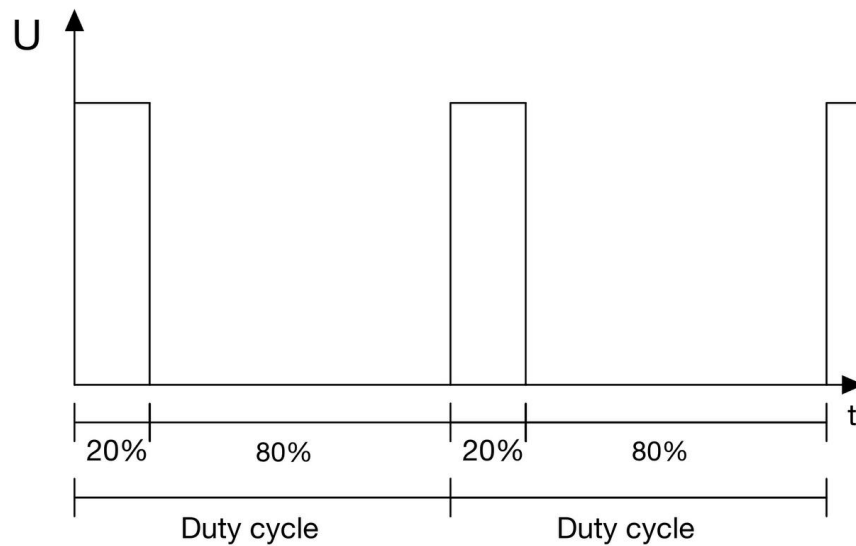In this work, the duty cycle was implemented on the MCP front voltage vmf.

Figure C.1: Scheme of a $20\,\%$ duty cycle - not to scale.

C.2 Schemes

A run can consist of several schemes. Fig. C.2 shows a visual example of such an division. Each scheme has the same beam parameters. The detector parameters change from scheme to scheme. Therefore, each scheme records the same data with different detector settings, e.g. the start time.

Most of the measurements consists of one scheme and do not need a such a segmentation. However, in Sec. 3.3.5 the run is split into five schemes.
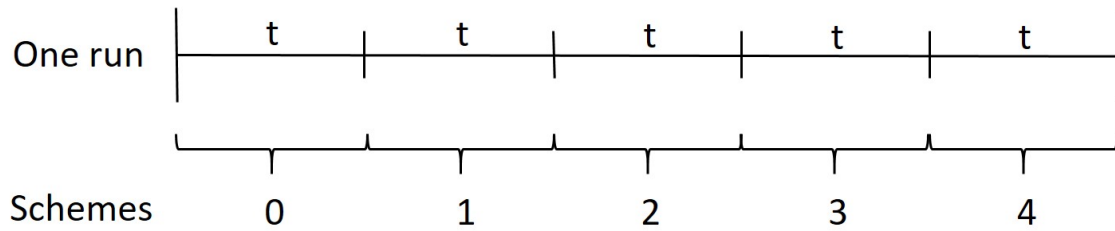

Figure C.2: Scheme of a run with five schemes. - not to scale.

D Parameters

A	$\left(\frac{120\,\mathrm{mm}}{2}\right)^2 \pi$
d	$1.5\,\mathrm{mm}$
ϵ_r	8.3
Open Area Ratio	$58\,\%$

Table D.1: MCP specifications based on [6].

Run	$U_{\mathrm{MCP_f}}$ [V]	$U_{\mathrm{MCP_b}}$ [V]	U_{P} [kV]
0003	-778	1000	11
0009	-778	1000	10
0010	-778	1000	9
0011	-778	1000	8
0012	-778	1000	7
0013	-778	1000	6
0014	-778	1000	5
0015	-778	1000	4
0016	-778	1000	3

Table D.2: Parameters of variation of the phosphor screen voltage (see 3.3.1).

Run	$U_{\mathrm{MCP_f}}$ [V]	$U_{\mathrm{MCP_b}}$ [V]	U_{P} [V]
0019	-1778	0	9222
0020	-1578	200	9422
0021	-1378	400	9622
0022	-1178	600	9822
0023	-978	800	10022
0026	-378	1400	10622
0027	-178	1600	10822
0029	-578	1200	10422
0030	-778	1000	10222

Table D.3: Parameters of shifting zeropoint (see 3.3.2).

Run	$U_{\mathrm{MCP_f}}$ [V]	$U_{\mathrm{MCP_b}}$ [V]	U_{P} [V]
0039	-778	1000	10700
0042	-778	1050	10750
0043	-778	1100	10800
0044	-778	1150	10850
0045	-778	1200	10900
0046	-778	1250	10950
0047	-778	1300	11000

Table D.4: Parameters for variation of MCP bias voltage (see sec. 3.3.3).

Run	$U_{\mathrm{MCP_f}}$ [V]	$U_{\mathrm{MCP_b}}$ [V]	U_{P} [V]	t_{stor} [s]	t_{boff} [s]	Inj. window [μs]
0050	-778	1000	10700	120	50	15,7
0051	-778	1100	10800	120	50	15,7
0052	-778	1200	10900	120	50	15,7

Table D.5: Parameters of saturation studies (see Sec. 3.3.5).

Run	$U_{\mathrm{MCP_f}}$ [V]	$U_{\mathrm{MCP_b}}$ [V]	U_{P} [V]	t_{off} [ms]	Inj. window [μs]	t_{width} [ms]
0059	-778	1000	10700	500	8,3	500
0060	-778	1000	10700	480	8,3	500
0061	-778	1000	10700	180	8,3	800
0062	-778	1000	10700	250	8,3	730
0063	-778	1000	10700	300	8,3	680
0064	-778	1000	10700	350	8,3	630
0065	-778	1000	10700	400	8,3	580
0066	-778	1000	10700	450	8,3	530
0067	-778	1000	10700	500	8,3	480
0068	-778	1000	10700	550	8,3	430
0069	-778	1000	10700	700	8,3	280
0070	-778	1000	10700	150	8,3	830
0071	-778	1000	10700	100	8,3	880
0073	-778	1000	10700	50	8,3	930
0074	-778	1000	10700	40	8,3	940
0075	-778	1000	10700	600	8,3	380
0076	-778	1000	10700	650	8,3	330

Table D.6: Parameters of switching behavior (see Sec. 3.4.1) at count rates of $\sim 10 \times 10^3 \, \mathrm{s}^{-1}$.

Run	$U_{\mathrm{MCP_f}}$ [V]	$U_{\mathrm{MCP_b}}$ [V]	U_{P} [V]	t_{off} [ms]	Inj. window [μs]	t_{width} [ms]
0077	-778	1000	10700	700	5,3	280
0078	-778	1000	10700	600	5,3	380
0079	-778	1000	10700	500	5,3	480
0080	-778	1000	10700	400	5,3	580
0081	-778	1000	10700	300	5,3	680
0082	-778	1000	10700	200	5,3	780
0083	-778	1000	10700	350	5,3	630
0084	-778	1000	10700	250	5,3	730
0085	-778	1000	10700	150	5,3	830
0086	-778	1000	10700	100	5,3	880
0087	-778	1000	10700	50	5,3	930

Table D.7: Parameters of switching behavior (see Sec. 3.4.1) at count rates of $\sim$ $6 \times 10^3\,\mathrm{s}^{-1}$.

Run	U_{MCP_f} [V]	U_{MCP_b} [V]	$U_{Pscreen}$ [V]	$U_{MCP_f}^{off}$ [V]	Inj. wind. [μs]	f	Duty cyc.
0158	-778	1000	10700	0	15,1	50	20
0159	-778	1000	10700	0	15,1	100	20
0160	-778	1000	10700	0	15,1	500	20
0161	-778	1000	10700	0	15,1	10	20

Table D.8: Variation of the switching frequency (see Sec. 3.4.2).

Run	U_{MCP_f} [V]	U_{MCP_b} [V]	$U_{Pscreen}$ [V]	$U_{MCP_f}^{off}$ [V]	Inj. wind. [μs]	f	Duty cyc.
0162	-778	1000	10700	0	15,1	50	1
0163	-778	1000	10700	0	15,1	50	5
0164	-778	1000	10700	0	15,1	50	20

Table D.9: Variation of the duty cycle (see Sec. 3.4.2 and 3.4.3).

Run	U_{MCP_f} [V]	U_{MCP_b} [V]	$U_{Pscreen}$ [V]	$U_{MCP_f}^{off}$ [V]	Inj. wind. [μs]	f	Duty cyc.
0165	-778	1000	10700	100	15,1	50	20
0166	-778	1000	10700	200	15,1	50	20
0167	-778	1000	10700	300	15,1	50	20
0168	-778	1000	10700	400	15,1	50	20
0169	-778	1000	10700	500	15,1	50	20
0170	-778	1000	10700	600	15,1	50	20
0171	-778	1000	10700	700	15,1	50	20

Table D.10: Variation of the switching voltage (see Sec. 3.4.2).

E Plots
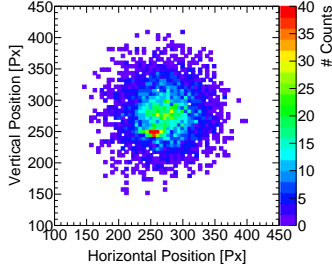
(a) $U_\mathrm{P} = 9222\,\mathrm{V}$
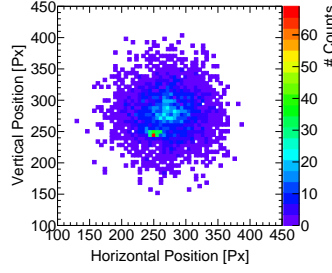
(b) $U_\mathrm{P} = 9422\,\mathrm{V}$
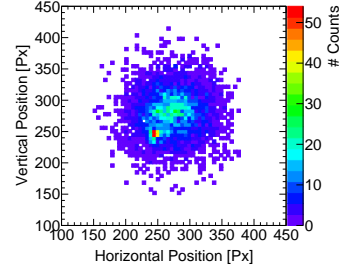
(c) $U_\mathrm{P} = 9622\,\mathrm{V}$
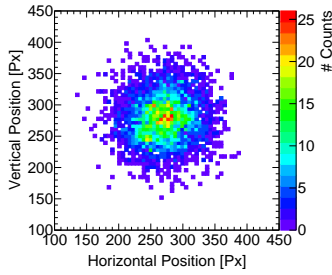
(d) $U_\mathrm{P} = 9822\,\mathrm{V}$
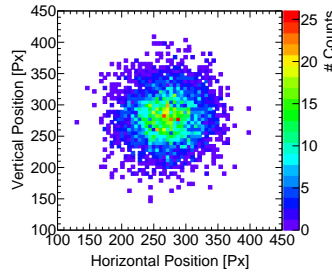
(e) $U_\mathrm{P} = 1022\,\mathrm{V}$
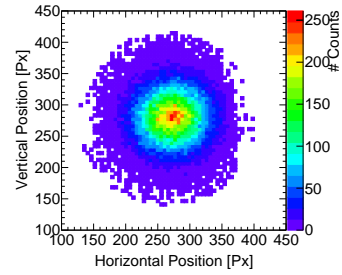
(f) $U_\mathrm{P} = 1222\,\mathrm{V}$
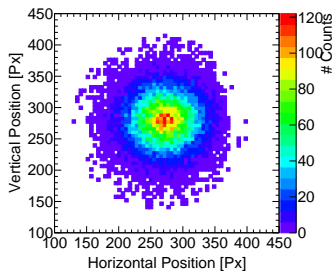
(g) $U_\mathrm{P} = 1422\,\mathrm{V}$
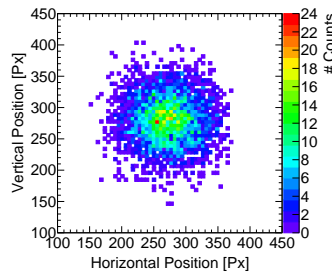
(h) $U_\mathrm{P} = 1622\,\mathrm{V}$
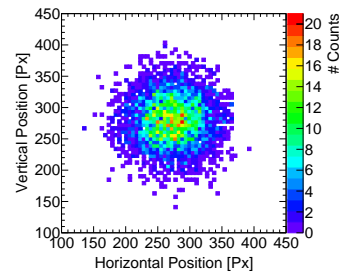
(i) $U_\mathrm{P} = 10\,822\,\mathrm{V}$

Figure E.1: 2D-double images of Sec. 3.3.2 for different pearameters.
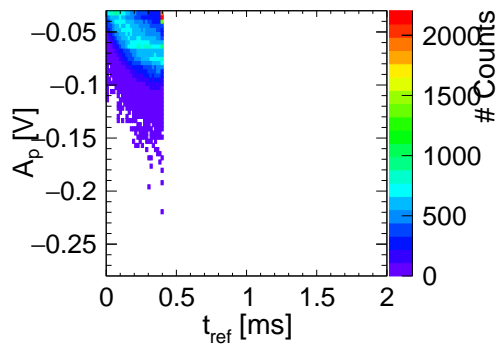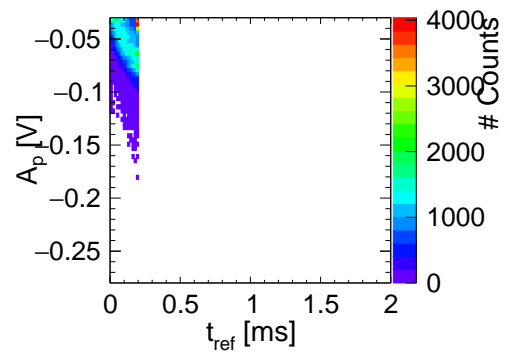
(a) $f = 500\,\mathrm{Hz}$, $d = 20\,\%$.
(b) $f = 50\,\mathrm{Hz}$, $d = 1\,\%$

Figure E.2: Time evolution plots for a detector on-time below 1 ms.

Part III

Appendix

F Bibliography

[1] ESA. Sputnik - mehr als bloß ein Satellit. `https://www.esa.int/Space_in_Member_States/Germany/Sputnik_-_mehr_als_bloss_ein_Satellit`. Last accessed on 29.05.2022.

[2] R. von Hahn, A. Becker, F. Berg, K. Blaum, C. Breitenfeldt, H. Fadil, F. Fellenberger, M. Froese, S. George, J. Göck, M. Grieser, F. Grussie, E. A. Guerin, O. Heber, P. Herwig, J. Karthein, C. Krantz, H. Kreckel, M. Lange, F. Laux, S. Lohmann, S. Menk, C. Meyer, P. M. Mishra, O. Novotný, A. P. OConnor, D. A. Orlov, M. L. Rappaport, R. Repnow, S. Saurabh, S. Schippers, C. D. Schröter, D. Schwalm, L. Schweikhard, T. Sieber, A. Shornikov, K. Spruck, S. Sunil Kumar, J. Ullrich, X. Urbain, S. Vogel, P. Wilhelm, A. Wolf, and D. Zajfman. The cryogenic storage ring CSR. *Review of Scientific Instruments*, 87(6):063115, 2016.

[3] S. S. Prasad and Jr. Huntress, W. T. A model for gas phase chemistry in interstellar clouds: I. The basic model, library of chemical reactions, and chemistry among C, N, and O compounds. , 43:1–35, May 1980.

[4] M. Larsson and A.E. Orel. *Dissociative Recombination of Molecular Ions*. Cambridge Molecular Science. Cambridge University Press, 2008.

[5] Julia Jäger. Implementation of a new setup for improved 3d imaging of neutral fragments at the cryogenic storage ring. Master's thesis, Ruprecht-Karls-Universität Heidelberg, 2021.

[6] Arno Becker. *Imaging of Neutral Fragmentation Products from Fast Molecular Ion Beams: Paving the Way for Reaction Studies in Cryogenic Environment.* PhD thesis, Ruprecht-Karls-Universität Heidelberg, 2016.

[7] Daniel Roman Paul. *Electron recombination studies of rotationally cold CH+ ions at the Cryogenic Storage Ring.* PhD thesis, Ruprecht-Karls-Universität Heidelberg, 2021.

[8] Lukas Berger. Analyse von rekombinationsprozessen von hochgeladenen ionen anhand einer flugzeitmessung in einer portablen elektronenstrahlionenfalle. Bachelor's thesis, Ruprecht-Karls-Universität Heidelberg, 2021.

[9] I.V Hertel and C.-P. Schulz. *Atome, Moleküle und optische Physik 2.* Springer-Verlag Berlin Heidelberg, 2010.

[10] A.S. Tremsin, J.F. Pearson, G.W. Fraser, W.B. Feller, and P. White. Microchannel plate operation at high count rates: new results. *Nuclear Instruments and Methods in Physics Research Section A: Accelerators, Spectrometers, Detectors and Associated Equipment*, 379(1):139–151, 1996.

[11] Joseph Ladislas Wiza. Microchannel plate detectors. *Nuclear Instruments and Methods*, 162(1):587–601, 1979.

[12] Proxi vision. Phosphor screens. https://www.proxivision.de/datasheets/Phosphor-Screen-PR-0056E-03.pdf. Last accessed on 29.05.2022.

[13] Endres Lukas. Cryogenic characterization of a microchannel plate detector. Master's thesis, Ruprecht-Karls-Universität Heidelberg, 2020.

[14] X. Urbain, D. Bech, J.-P. Van Roy, M. Géléoc, S. J. Weber, A. Huetz, and Y. J. Picard. A zero dead-time multi-particle time and position sensitive detector based on correlation between brightness and amplitude. *Review of Scientific Instruments*, 86(2):023305, 2015.

[15] Lutz Lammich. *Fragmentation Studies with Stored Beams of Small Polyatomic Ion*. PhD thesis, Ruprecht-Karls-Universität Heidelberg, 2004.

[16] P. Møller. Beam-residual gas interactions. (OPEN-2000-277), 1999.

[17] Daniel Paul. Beam time 2018 week 3 o+ analysis. Technical report, Max-Planck-Institur für Kernphysik Heidelberg, 2018.

[18] CERN. Chapter: Fittinghistograms. https://root.cern.ch/root/htmldoc/guides/users-guide/FittingHistograms.html#the-tf1-function-class. Last accessed on 30.05.2022.

[19] L. Gamer, D. Schulz, C. Enss, A. Fleischmann, L. Gastaldo, S. Kempf, C. Krantz, O. Novotný, D. Schwalm, and A. Wolf. MOCCA: A 4k-Pixel Molecule Camera for the Position- and Energy-Resolving Detection of Neutral Molecule Fragments at CSR. *Journal of Low Temperature Physics*, 184(3-4):839–844, August 2016.

[20] O. Novotný, S. Allgeier, C. Enss, A. Fleischmann, L. Gamer, D. Hengstler, S. Kempf, C. Krantz, A. Pabinger, C. Pies, D. W. Savin, D. Schwalm, and A. Wolf. Cryogenic micro-calorimeters for mass spectrometric identification of neutral molecules and molecular fragments. *Journal of Applied Physics*, 118(10):104503, 2015.

[21] J.H. Gross. *Massenspektrometrie*. Springer-Verlag Berlin Heidelberg, 2013.

Erklärung:

Ich versichere, dass ich diese Arbeit selbstständig verfasst habe und keine anderen als die angegebenen Quellen und Hilfsmittel benutzt habe.

Heidelberg, den (Datum)   31.05.2022 *Selina Gair*